

Efficient chemical fixation of CO₂ from direct air under environment-friendly co-catalyst and solvent-free ambient conditions

Rajesh Das,¹ Thirumavalavan Ezhil,¹ Athulya S. Palakkal,² D. Muthukumar,² Renjith S.

Pillai² and C. M. Nagaraja*¹

¹Department of Chemistry, Indian Institute of Technology Ropar, Rupnagar 140001,

Punjab, India. Tel: 91-1881-242229. Email: cmnraja@iitrpr.ac.in

²Department of Chemistry, Faculty of Engineering and Technology, SRM Institute of Science and Technology, Kattankulathur 603203, Chennai, Tamil Nadu, India

Table of Contents

Sl. No.	Figure/ Table No.	Title	Page No.
1.		Materials and methods	S6-S7
2.		Synthesis of 4,4',4''-s-triazine-1,3,5-triyltri-p-aminobenzoic acid (H ₃ TATAB) ligand.	S7
3.	Scheme S1.	Synthesis scheme of 4',4''-s-triazine-1,3,5-triyltri-p-aminobenzoic acid (H ₃ TATAB) ligand.	S7
4.		Synthesis of Mg-MOF	S8
5.	Figure S1.	PXRD patterns of Mg-MOF (a) simulated pattern from single-crystal X-ray structure, (b) as-synthesized sample (c) activated sample, and (d) recycled sample after tenth catalytic cycle.	S8
6.	Figure S2.	FT-IR spectrum of Mg-MOF (a) activated and (b) recycled sample after tenth catalytic cycle.	S9
7.	Figure S3.	UV-Vis spectra of (a) H ₃ TATAB ligand, (b) activated Mg-MOF, (c) recycled sample after tenth catalytic cycle.	S9
8.		Adsorption measurements	S10

9.		Catalytic cycloaddition reactions of CO ₂ with epoxides	S10
10.		X-ray Crystallography	S11
11.	Figure S4.	TOPOS image of Mg-MOF.	S12
12.	Figure S5.	(a) View of 20-connected Mg1 node and (b) 11-connected Mg2 node.	S12
13.	Table S1.	Crystal data and structure refinement parameters for Mg-MOF.	S13
14.	Table S2.	Selected bond length (Å) and angles (°) for Mg-MOF.	S14
15.	Table S3.	Selected hydrogen bonding geometry for Mg-MOF.	S14
16.	Figure S6.	TGA plots of (a) as-synthesized, (b) solvent exchanged, and (c) activated Mg-MOF.	S15
17.	Figure S7.	PXRD patterns of Mg-MOF recovered after treating with various solvents (a) simulated pattern, sample treated with (b) DMF, (c) water, (d) acetone, (e) ethanol, (f) dichloromethane, and (g) methanol.	S15
18.		Analysis of gas adsorption isotherms	S16-S17
19.	Figure S8.	Carbon dioxide adsorption isotherm of Mg-MOF carried out at 273 K (a) and 298 K (b).	S17
20.	Figure S9.	Simulated and experimental adsorption enthalpy for CO ₂ in Mg-MOF.	S17
21.	Table S4.	Comparison of interaction energy (Q_{st}) with various reported Mg-based MOFs.	S18
22.	Figure S10.	(a) Comparison of the single component simulated isotherms for N ₂ (closed triangle) with the experimental data (closed circle) in Mg-MOF at 273 and 298 K and (b) simulated and experimental adsorption enthalpy for N ₂ in Mg-MOF.	S18
23.	Figure S11.	(a) Comparison of the single component simulated isotherms for O ₂ (closed triangle) with the experimental data (closed circle) in Mg-MOF at 273 and 298 K and (b) simulated and experimental	S19

		adsorption enthalpy for O ₂ in Mg-MOF.	
24.	Figure S12.	Calculation of gas selectivity constant for (a) CO ₂ and (b) N ₂ and (c) O ₂ gases using on Henry law.	S19
25.		COMPUTATIONAL MODELLING PART	S20
26.		MICROSCOPIC MODELS FOR THE HOST FRAMEWORK	S20
27.	Figure S13.	The single unit cell (1×1×1 simulation box) of Mg-MOF considered for the DFT calculations, viewed along <i>c</i> -direction (black, carbon; grey, hydrogen; red, oxygen; green, Magnesium).	S20-S21
28.		DFT DERIVED SPECIFIC FORCEFIELDS	S21-S22
29.	Figure S14.	DFT geometry optimization of Mg-MOF with (a) CO ₂ , (b) N ₂ , and (c) O ₂ loaded.	S22
30.	Figure S15.	The potential energy values are calculated as moving each molecule along the dashed line, (a) C _{CO2} , (b) O _{CO2} , (c) N _{N2} , and (d) O _{O2} (comparison of DFT-derived forcefield fitted curve (red circles) on the DFT interaction energy profile (black squares)).	S23
31.	Table S5.	The DFT based binding energy calculated with PBE functional by MOF and guest interaction.	S23
32.	Table S6.	LJ potential parameters for the atoms of the Mg-MOF.	S24
33.	Table S7.	Potential parameters and partial charges for the adsorbates.	S24
34.	Table S8.	Buckingham parameters associated with the Mg-MOF and adsorbates.	S25
35.		GCMC Simulations	S25-S26
36.		Computational predictions–single adsorption isotherm	S27
37.		RADIAL DISTRIBUTION FUNCTION	S27
38.	Figure S16.	Radial distribution functions (RDF) between CO ₂ and the atoms of the MOF framework (Organic nitrogen,	S28

		N_{TATAB} : blue, Organic hydrogen, H_{TATAB} : Magenta and Organic Oxygen, O_{TATAB} : green, Organic carbon, C_{TATAB} : black, Magnesium, Mg: red) extracted from the single-component adsorption in Mg-MOF in 0.01 bar at 273 K.	
39.	Figure S17.	Radial distribution functions (RDF) between N_2 and the atoms of the MOF framework (Organic nitrogen, N_{TATAB} : blue, Organic hydrogen, H_{TATAB} : Magenta and Organic Oxygen, O_{TATAB} : green, Organic carbon, C_{TATAB} : black, Magnesium, Mg: red) extracted from the single-component adsorption in Mg-MOF in 0.01bar at 273 K (a) and 298 K (b).	S28
40.	Figure S18.	Radial distribution functions (RDF) between O_2 and the atoms of the MOF framework (Organic nitrogen, N_{TATAB} : blue, Organic hydrogen, H_{TATAB} : Magenta and Organic Oxygen, O_{TATAB} : green, Organic carbon, C_{TATAB} : black, Magnesium, Mg: red) extracted from the single-component adsorption in Mg-MOF in 0.01bar at 298K.	S29
41.	Figure S19.	1H NMR ($CDCl_3$, 400 MHz) spectra for the cycloaddition reaction of epichlorohydrin (ECH) with CO_2 using Mg-MOF as catalyst.	S29
42.	Figure S20.	1H NMR ($CDCl_3$, 400 MHz) spectra for the cycloaddition reaction of epichlorohydrin (ECH) with CO_2 using $Mg(NO_3)_2 \cdot 6H_2O$ metal salt as catalyst.	S30
43.	Figure S21.	1H NMR ($CDCl_3$, 400 MHz) spectra for the cycloaddition reaction of epichlorohydrin (ECH) with CO_2 using H_3TATAB ligand as catalyst.	S30
44.	Figure S22.	1H NMR ($CDCl_3$, 400 MHz) spectra for the cycloaddition reaction of 1,2-epoxypropane with CO_2 using Mg-MOF as the catalyst.	S31

45.	Figure S23.	¹ H NMR (CDCl ₃ , 400 MHz) spectra for the cycloaddition reaction of 1,2-epoxybutane with CO ₂ using Mg-MOF as catalyst.	S31
46.	Figure S24.	¹ H NMR (CDCl ₃ , 400 MHz) spectra for the cycloaddition reaction of 1,2-epoxyhexane with CO ₂ using Mg-MOF as catalyst.	S32
47.	Figure S25.	¹ H NMR (CDCl ₃ , 400 MHz) spectra for the cycloaddition reaction of 1,2-epoxydecane with CO ₂ using Mg-MOF as catalyst.	S32
48.	Table S9.	Optimized geometries of epoxides using Gaussian09 at b3lyp/6-311g (d,p) level.	S33
49.	Figure S26.	¹ H NMR (CDCl ₃ , 400 MHz) spectra for the cycloaddition reaction of butyl glycidyl ether with CO ₂ using Mg-MOF as catalyst.	S34
50.	Figure S27.	¹ H NMR (CDCl ₃ , 400 MHz) spectra for the cycloaddition reaction of allyl glycidyl ether with CO ₂ using Mg-MOF as a catalyst.	S34
51.	Figure S28.	¹ H NMR (CDCl ₃ , 400 MHz) spectra for the cycloaddition reaction of styrene oxide with CO ₂ using Mg-MOF as a catalyst.	S35
52.	Figure S29.	¹ H NMR (CDCl ₃ , 400 MHz) spectra for the cycloaddition reaction of ECH with simulated dry flue gas, CO ₂ :N ₂ (13: 87%) using Mg-MOF as catalyst.	S35
53.	Figure S30.	¹ H NMR (CDCl ₃ , 400 MHz) spectra for the cycloaddition reaction of ECH with CO ₂ using direct air for 24 h.	S36
54.	Figure S31.	¹ H NMR (CDCl ₃ , 400 MHz) spectra for the cycloaddition reaction of ECH with CO ₂ using direct air for 48 h.	S36
55.		MULTICOMPONENT ADSORPTION	S37
56.	Figure S32.	Maps of the occupied positions of CO ₂ (a), N ₂ (b), and O ₂ (c) in 500 equilibrated frames for a given pressure of 1 bar and at 298 K for Mg-MOF, color code for the	S37

		atoms: C (black), Mg (green), O (red), H (grey), and N(blue).	
57.		Selectivity O ₂ /(N ₂ +O ₂)	S38
58.	Figure S33.	Selectivity plot of CO ₂ /(O ₂ + N ₂) in presence of RH = 1.57% at 298 K.	S38
59.	Figure S34.	CO ₂ adsorption isotherms at various relative humidity of pre-humidified Mg-MOF at 298K.	S38
60.	Figure S35.	Simulated selectivity of CO ₂ /(O ₂ +N ₂) in various pre-humidified air at 1bar.	S39
61.	Figure S36.	¹ H NMR (CDCl ₃ , 400 MHz) spectra for the cycloaddition reaction of ECH with CO ₂ using Mg-MOF recycled after ten cycles of catalysis.	S39
62.	Figure S37.	MP-AES calibration curve.	S40
63.	Figure S38.	Unit crystal (left) and primitive (right) structure of Mg-MOF obtained through optimization via DFT method viewed along <i>a</i> vector direction.	S40
64.	Figure S39.	Mechanistic Pathways of the Intermediates and Transition States in the Cycloaddition of Propylene oxide and CO ₂ using the HbMOF1 catalyst (Bond Distances are in Å).	S41
65.	Figure S40.	FT-IR spectra of (a) Mg-MOF, (b) epichlorohydrin, and (c) Mg-MOF treated with epichlorohydrin.	S41
66.		References	S42-S46

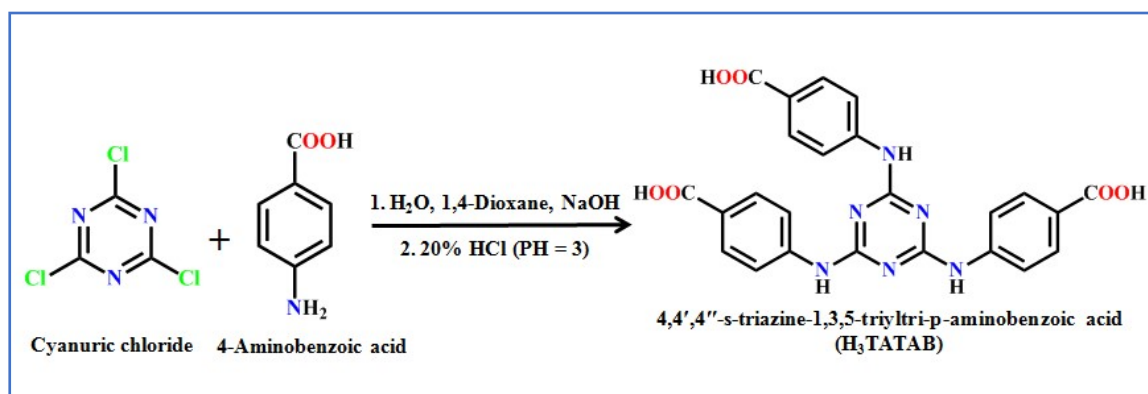
Materials and methods

All reagents used in this study were commercially available and used as received without further purification. Mg(NO₃)₂·6H₂O, 4-aminobenzoic acid, and cyanuric chloride were

purchased from Sigma Aldrich Chemical Co. Sodium hydroxide and sodium bicarbonates were purchased from SD file Co. Thermogravimetric analysis (TGA) of Mg-MOF was carried out on Mettler Toledo Thermogravimetric Analyzer in the N₂ atmosphere (flow rate of 50 mL min⁻¹) in the temperature range of 30-800 °C (heating rate of 5 °C min⁻¹). The phase-purity of the MOF samples was confirmed by powder XRD recorded on a PANalytical's X'PERT PRO diffractometer using CuK_α radiation (k = 1.542 Å; 40 kV, 20 MA). Fourier transform infrared (FT-IR) spectra of the samples were recorded on Perkin Elmer FTIR spectrometer.

Synthesis of 4,4',4''-s-triazine-1,3,5-triyltri-p-aminobenzoic acid (H₃TATAB) ligand.

The 4,4',4''-s-triazine-1,3,5-triyltri-p-aminobenzoic acid (H₃TATAB) ligand was synthesized by following the previously reported literature procedure with a slight modification.¹ Briefly, a solution of 4-aminobenzoic acid (1.8 g, 13.3 mmol) in 20 mL of water and 3 mL of 5N sodium hydroxide was charged with sodium bicarbonate (0.9 g, 11.0 mmol). To this solution, cyanuric chloride (0.6 g, 3.3 mmol) in 50 mL of 1,4-Dioxane was added dropwise and stirred for 15 min. The resulting reaction mixture was refluxed overnight then cooled to room temperature and acidified by 20% hydrochloric acid (HCl) to attain pH of 3 (Scheme S1). The resulting precipitate was neutralized by washing with water. ¹H NMR DMSO-d₆, δ: 12.55 (s, 3H), 9.84 (s, 3H), 7.97 (d, 2H) and 7.87 (d, 6H).



Sch

eme S1. Synthesis scheme of 4,4',4''-s-triazine-1,3,5-triyltri-p-aminobenzoic acid (H₃TATAB) ligand.

Synthesis of Mg-MOF

The Mg-MOF was synthesized by following solvothermal route at 120 °C (Scheme 1). The 4,4',4''-s-triazine-1,3,5-triyltri-p-aminobenzoic acid (H₃TATAB) ligand (0.075 mmol, 36.48 mg) was dissolved in 6 mL of DMF in a glass vial. To this solution, 3mL ethanol solution of Mg(NO₃)₂·6H₂O (0.112 mmol, 30 mg) was added dropwise with stirring. The resulting clear solution was heated in a preheated oven at 120 °C for 4 days. After 4 days colorless rod-like crystals of Mg-MOF was obtained. The phase purity of the as-synthesized sample was confirmed by powder X-ray diffraction analysis (Figure S1). FTIR (cm⁻¹): 3380 (w), 2979 (w), 1592 (m), 1486 (m), 1373 (s), 1238 (m), 1179 (m), 1.97 (m), 853 (w), 784 (m), 702 (w) (Figure S2). The elemental analysis, calculated (%) for as-synthesized {Mg₃(TATAB)₂(HCOO)(H₂O)₆(DMF)₃(DMA)}_n (C₆₀H₇₂N₁₆O₂₃Mg₃) Calculated: C:49.42, H:4.98, N:15.37 and found C:49.21, H:4.82, N:15.19. Activated sample {Mg₃(TATAB)₂(HCO₂)(DMA)}_n, (C₅₁H₃₉N₁₃O₁₄Mg₃) Calculated: C:50.59, H:3.25, N:15.04 and found C:54.01, H:2.98, N:15.23.

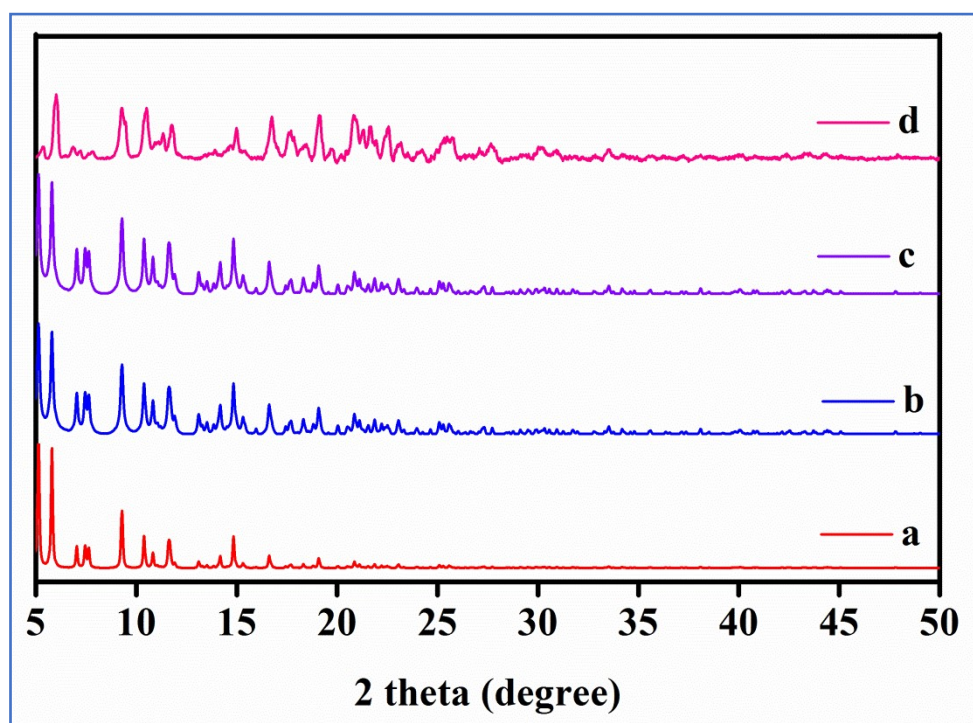


Figure S1. PXRD patterns of Mg-MOF (a) simulated pattern from single-crystal X-ray structure, (b) as-synthesized sample, (c) activated sample, and (d) recycled sample after tenth catalytic cycle.

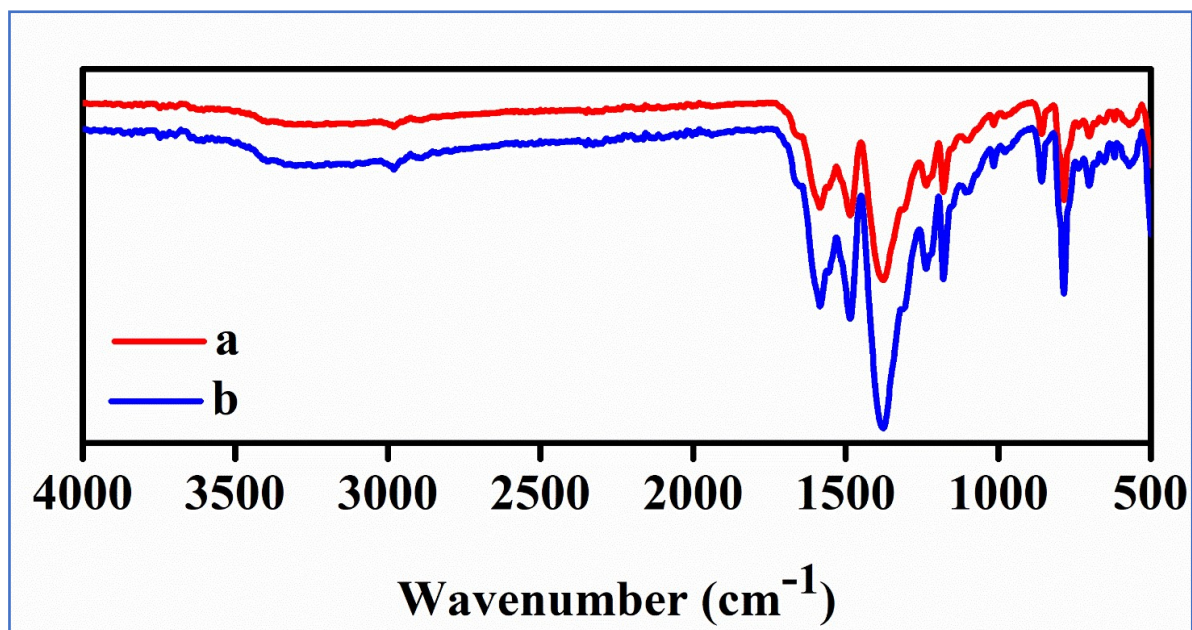


Figure S2. FT-IR spectra of Mg-MOF, (a) activated and (b) recycled sample after tenth catalytic cycle.

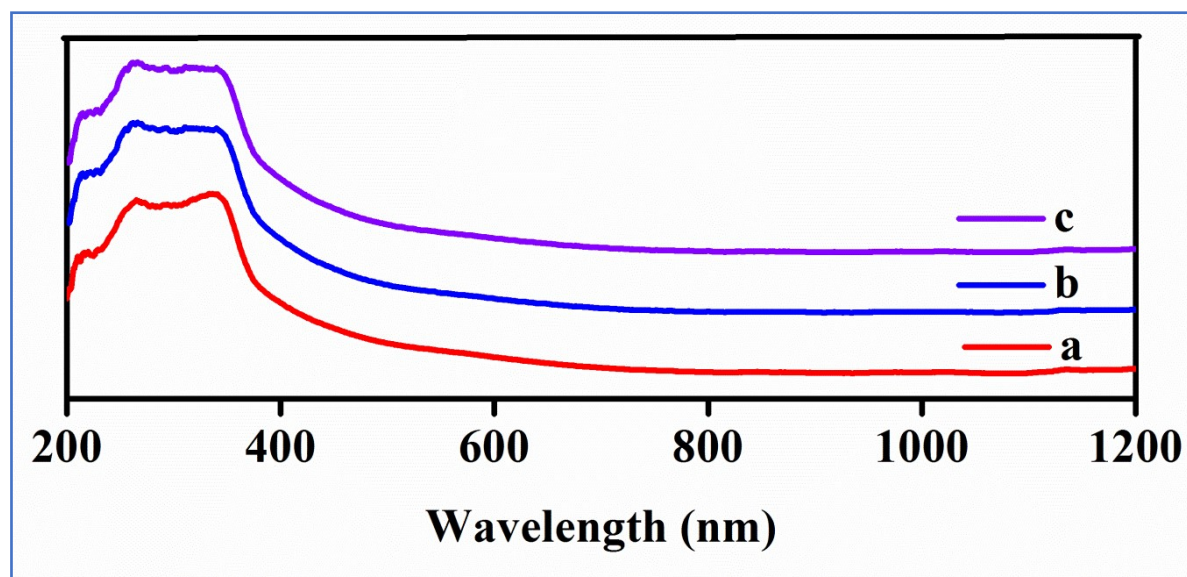


Figure S3. UV-Vis spectra of (a) H₃TATAB ligand, (b) activated Mg-MOF, (c) recycled sample after ten catalytic cycles.

Adsorption measurements

N₂ adsorption-desorption measurements were performed at 77 K while CO₂ adsorption-desorption measurements were carried out at 273 and 298 K on a Quantachrome QUADRASORB-SI automatic volumetric instrument. Ultrapure (99.995%) N₂ and CO₂ gases were used for the isotherm measurements. Before starting the adsorption measurements, the MOF sample (0.10 g) was exchanged with acetone for 3 days and further outgassed at 130 °C under vacuum for 15 h, then the activated sample was connected to the surface area analyzer and all the operations were computer-controlled. 273 and 298 K temperatures were achieved by using water and ethylene glycol mixture (1:1 v/v mixture) using a chiller. Whereas, 77 K was achieved by using liquid nitrogen. The dead volume of the sample cell was determined using He gas (99.995%).

Catalytic cycloaddition reactions of CO₂ with epoxides

The cycloaddition reactions of CO₂ with various epoxides were carried out in Schlenk tube. Prior to catalytic reactions, the Mg-MOF was exchanged with acetone and activated at 130 °C for 15 h under vacuum to remove guest solvent molecules. In a typical reaction, the epoxide (20 mmol), and the activated MOF catalyst (0.1 mol%) were taken in the Schlenk tube at room temperature. Then, CO₂ (1 atm) was introduced using a balloon and the reaction mixture was allowed to stir at 60 °C for 24 h. After which time, the mixture was cooled to RT and the catalyst was separated from the reaction mixture by simple centrifugation and the catalytic conversions were determined from ¹H NMR spectra of the filtrate. The recovered catalyst was washed with acetone thoroughly and activated at 130 °C under vacuum for 15 h and reused for subsequent catalytic cycles. A similar procedure was employed for the catalytic reactions carried out with direct air, except that the CO₂ (balloon) was replaced by laboratory air with a continuous bubbling.

X-ray Crystallography

Single crystal X-ray structural data of Mg-MOF was collected on a CMOS based Bruker D8 Venture PHOTON 100 diffractometer equipped with an INCOATEC micro-focus source and graphite monochromated Mo K α radiation ($\lambda = 0.71073 \text{ \AA}$) operating at 50 kV and 30 mA. The SAINT² program was used for the integration of diffraction profiles and the absorption correction was made with the SADABS program.³ The structures were solved by SIR 92⁴ and refined by full-matrix least square method using SHELXL-2018⁵ and WinGX system, Version 2013.3.⁶ The non-hydrogen atoms in all the structures were located from the difference Fourier map and refined anisotropically. All the hydrogen atoms were fixed by HFIX and placed in ideal positions and included in the refinement process using a riding model with isotropic thermal parameters. The disordered guest DMF molecules and dimethylamine cation were treated with the SQUEEZE option of PLATON⁷ software. Hence the formula of the MOF was established based on TGA and elemental analysis. The potential solvent accessible area or void space was calculated using the PLATON software. All the crystallographic and structure refinement data of the Mg-MOF are summarized in Table S1. Selected bond lengths and angles are given in Table S2 and selected hydrogen bond details are summarized in Table S3. The crystallographic information file is deposited with CCDC number 2036640.

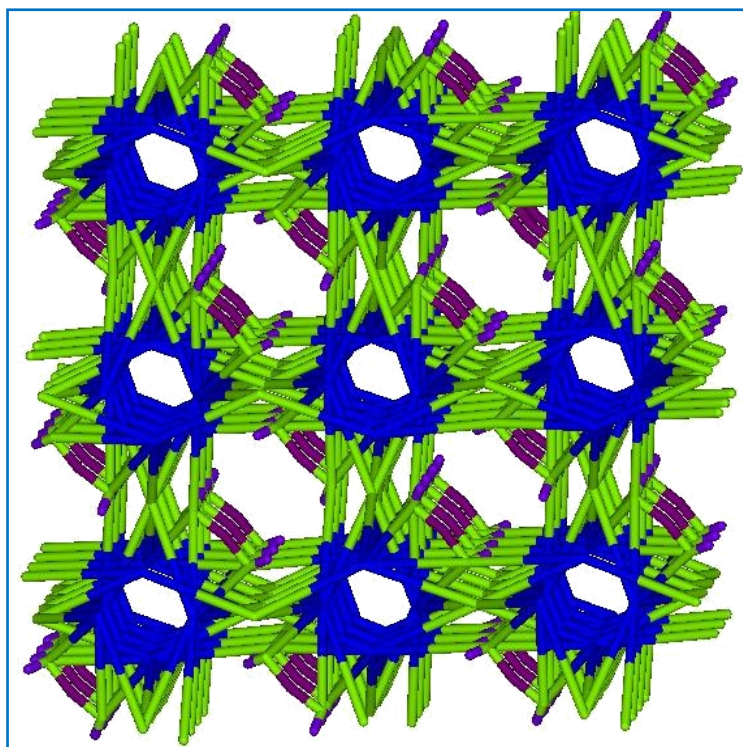


Figure S4. TOPOS image of Mg-MOF.

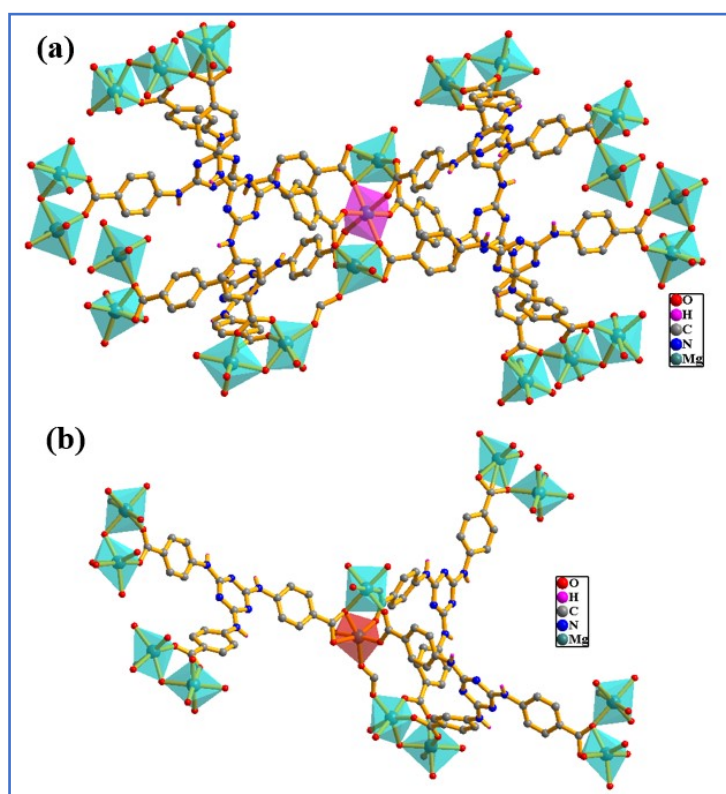


Figure S5. (a) View of 20-connected Mg1 node and (b) 11-connected Mg2 node.

Table S1. Crystal data and structure refinement parameters for Mg-MOF.

Parameters	Mg-MOF
Empirical formula	C ₆₀ H ₇₂ Mg ₃ N ₁₆ O ₂₃
Formula mass	1458.22
Crystal system	Orthorhombic
Space group	<i>Fddd</i>
a/ Å	16.9502(11)
b/ Å	47.376(3)
c/ Å	50.434(3)
α (degree)	90
β (degree)	90
γ (degree)	90
V (Å ³)	40500(4)
Z	16
M (mm ⁻¹)	0.072
F (000)	9360
T (K)	298
λ (Mo Kα) (Å)	0.71073
θ _{min} (deg)	2.4
θ _{max} (deg)	25.0
total data	183673
unique data	8915
R _{int}	0.083
Data [I > 2σ(I)]	6182
R ₁	0.0947
wR ₂	0.3374
S	1.34
CCDC	2036640

$${}^aR_1 = \frac{\sum ||F_o| - |F_c||}{\sum |F_o|}, \quad {}^b wR_2 = [\frac{\sum w(F_o^2 - F_c^2)^2}{\sum w(F_o^2)^2}]^{1/2}$$

Table S2. Selected bond length (Å) and angles (°) for Mg-MOF.

X-Y	Bond length (Å)	X-Y-Z	Bond angle (°)
Mg1-O5	2.060(3)	O1-Mg2-O2	94.91(15)
Mg1-O6	2.116(3)	O1-Mg2-O1w	175.45(18)
Mg1-O7	2.061(3)	O1-Mg2-O4	95.74(17)
Mg2-O1	1.999(4)	O1-Mg2-O6	97.17(14)
Mg2-O2	2.178(4)	O1-Mg2-O3	91.10(17)
Mg2-O1w	2.134(5)	O2-Mg2-O3	84.04(18)
Mg2-O4	1.989(4)	O2-Mg2-O4	158.25(18)
Mg2-O6	2.115(3)	O2-Mg2-O6	61.46(13)
Mg2-O3	2.124(5)	O2-Mg2-O3	98.89(17)
		O3-Mg2-O4	86.71(19)
X-Y-Z	Bond angle (°)	O3-Mg2-O6	86.25(16)
O5-Mg1-O6	88.60(11)	O3-Mg2-O3	84.69(19)
O5-Mg1-O7	88.33(12)	O4-Mg2-O6	98.37(16)
O6-Mg1-O7	90.34(11)	O4-Mg2-O3	99.80(19)

Table S3. Selected hydrogen bonding geometry for Mg-MOF.

D-H··A	H··A	D··A	D-H··A
N1-H1··N3	2.2000	3.056(5)	174.00
C5-H5··N2	2.3900	2.964(7)	119.00
C11-H11··N4	2.4100	2.974(7)	119.00
C14-H14··O5	2.4700	3.364(6)	161.00
C20-H20··N2	2.4800	2.925(7)	110.00

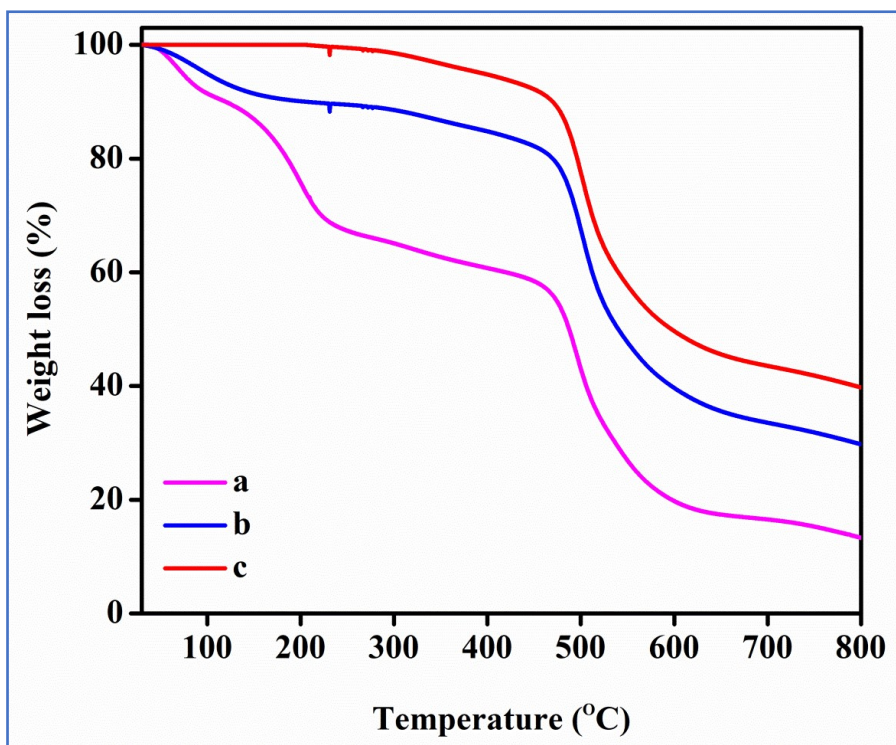


Figure S6. TGA plots of Mg-MOF (a) as-synthesized, (b) solvent exchanged, and (c) activated MOF.

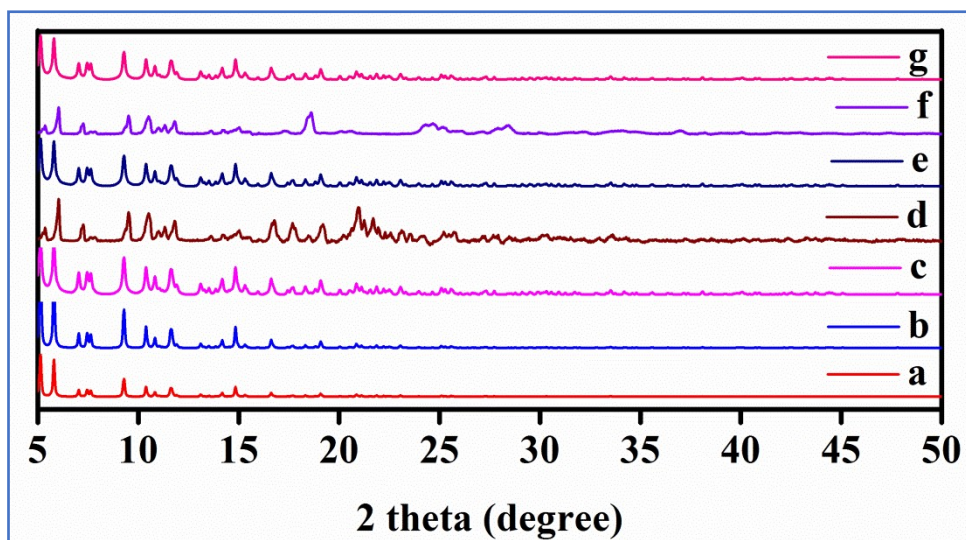


Figure S7. PXRD patterns of Mg-MOF recovered after treating with various solvents (a) simulated pattern and the sample treated with (b) DMF, (c) water, (d) acetone, (e) ethanol, (f), and (g) methanol.

Analysis of gas adsorption isotherms

Clausius-Clapeyron equation⁸ was used to calculate the enthalpies of carbon dioxide adsorption and by using Langmuir Freundlich equation⁹ an accurate fit was retrieved to get a precise prediction of CO₂ adsorbed at saturation. A modification of the Clausius-Clapeyron equation was used for the calculations.

$$\ln(P_1/P_2) = \Delta H_{ads}(T_2 - T_1/R.T_1.T_2) \dots\dots(i)$$

where P₁ and P₂ = Pressures for isotherm at 273 K and 298 K, respectively.

T₁ and T₂ = Temperatures for isotherm at 273 K and 298 K, respectively.

ΔH_{ads} = Enthalpy of adsorption.

R = Universal gas constant = 8.314 J/K/mol.

The pressure is a function of the amount of gas adsorbed which was determined by using Langmuir-Freundlich fit.

$$Q/Q_m = B.P^{(1/t)}/1 + (B.P^{(1/t)}) \dots\dots(ii)$$

where Q = moles of gas adsorbed.

Q_m = moles of gas adsorbed at saturation.

B and t = constants.

P = Pressure.

By rearranging equation (ii) we get equation (iii)

$$P = [(Q/Q_m)/\{B - (B.(Q/Q_m))\}]^t \dots\dots(iii)$$

Substituting equation (iii) into equation (i) we get

$$\Delta H_{ads} = \{R.T_1.T_2/(T_2 - T_1)\} \cdot \ln \frac{[(Q/Q_{m1})/\{B - (B.Q/Q_{m1})\}]^{t1}}{[(Q/Q_{m2})/\{B - (B.Q/Q_{m2})\}]^{t2}} \dots\dots(iv)$$

In equation (iv), subscripts 1 and 2 represent data corresponding to 273 K and 298 K, respectively.

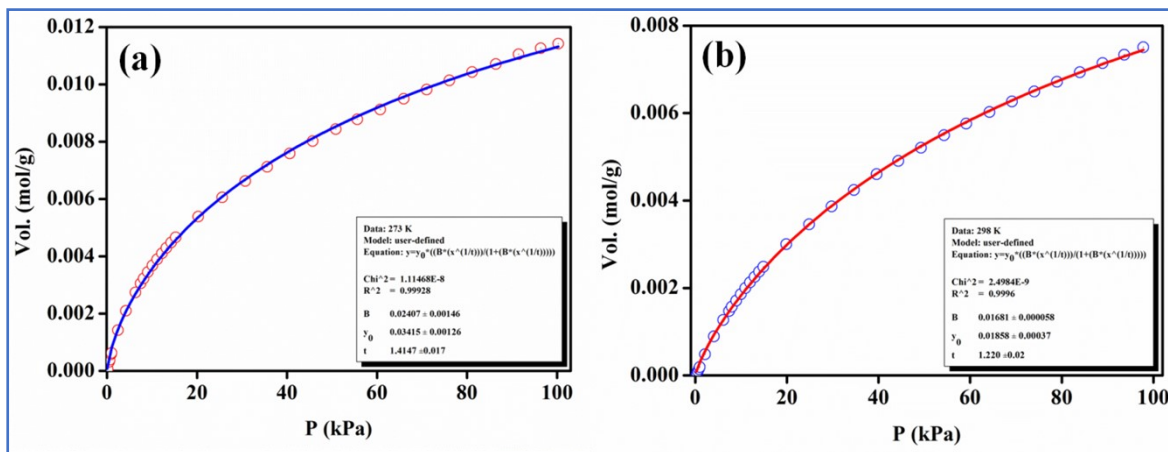


Figure S8. Carbon dioxide adsorption isotherm of Mg-MOF carried out at 273 K (a) and 298 K (b). The solid line shows the best fit to the data using the Langmuir-Freundlich equation.

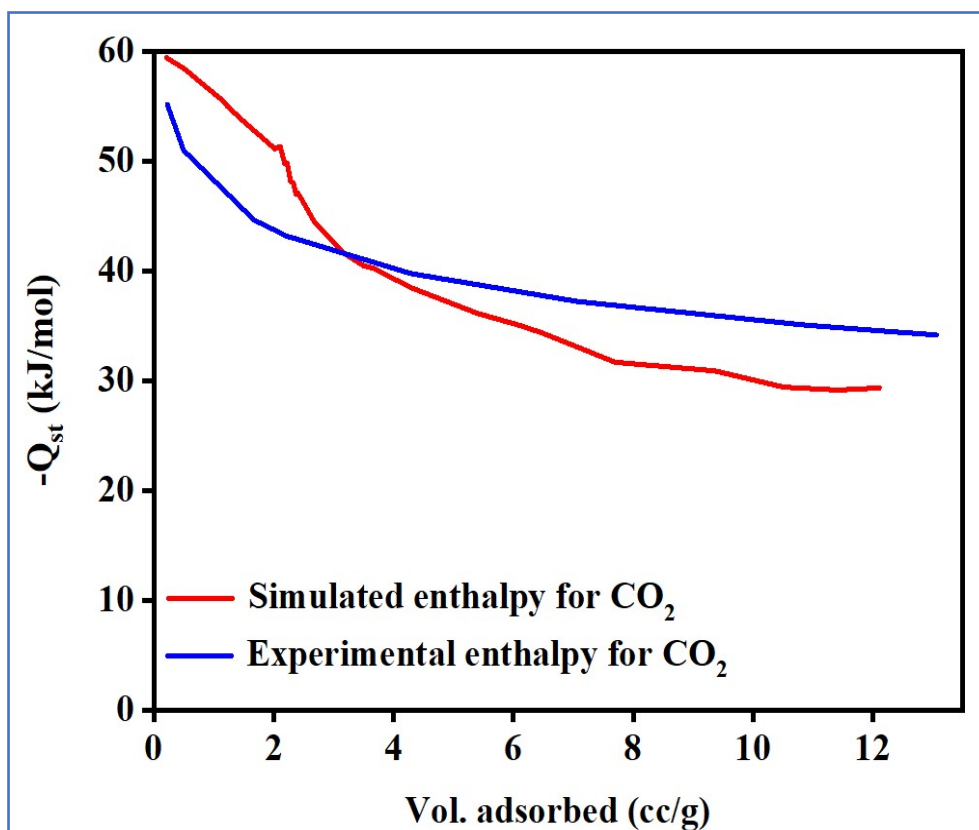


Figure S9. Simulated and experimental adsorption enthalpy for CO₂ in Mg-MOF.

Table S4. Comparison of interaction energy (Q_{st}) with various reported Mg-based MOF.

SL. No	MOF	Q_{st} (kJ/mol)	Reference
1	Mg-MOF-74(S)	42	10
2	Mg-MOF-184	35	11
3	[Mg ₂ (DOBDC)]	44	12
4	MOF-889	28	13
5	Mg-MOF-74	41	14
6	Mg-MOF-74 (pellets)	45	15
7	Mg-MOF	55	This work

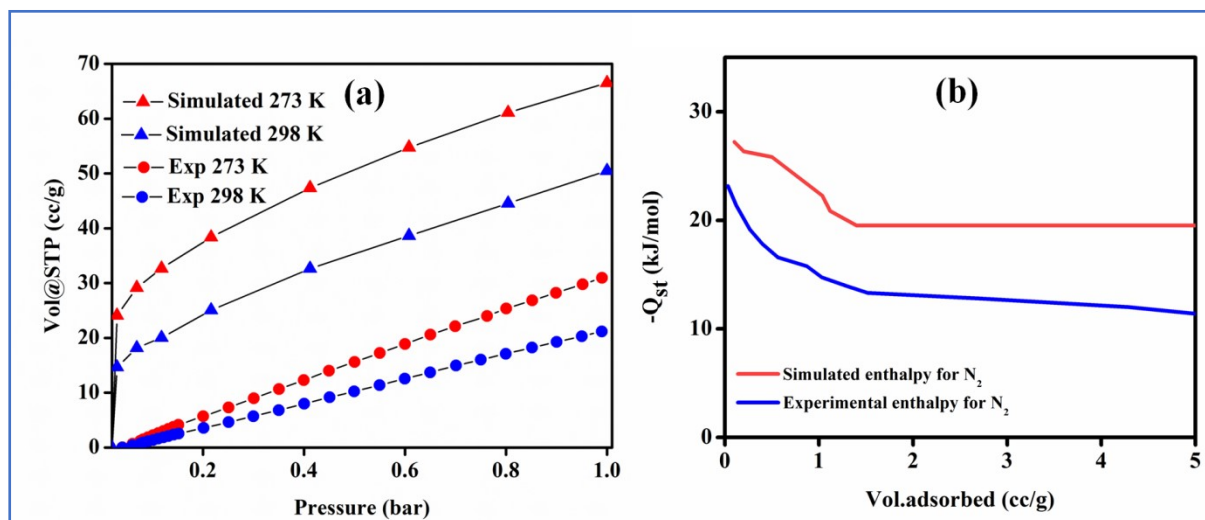


Figure S10. (a) Comparison of the single component simulated isotherms for N₂ (closed triangle) with the experimental data (closed circle) in Mg-MOF at 273 and 298 K and (b) Simulated and experimental adsorption enthalpy for N₂ in Mg-MOF.

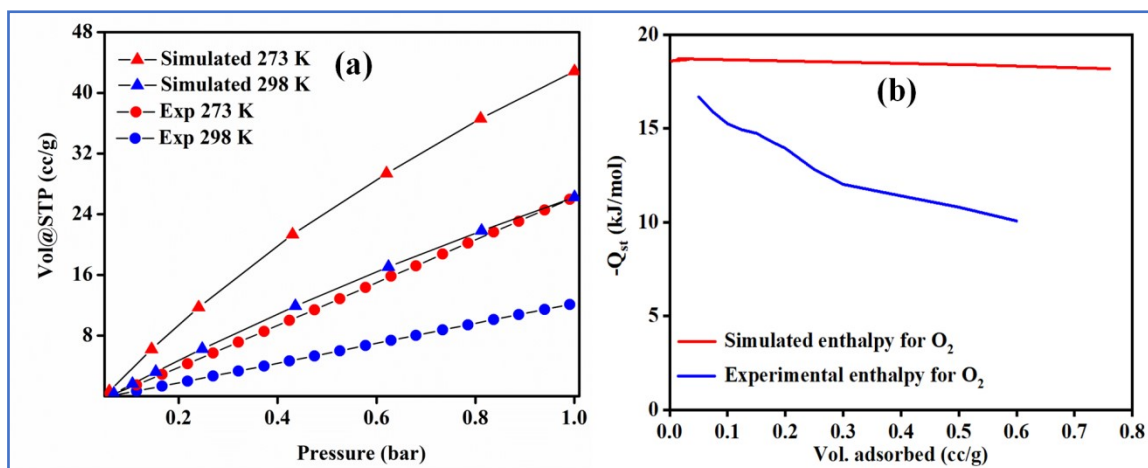


Figure S11. (a) Comparison of the single component simulated isotherms for O₂ (closed triangle) with the experimental data (closed circle) in Mg-MOF at 273 and 298 K and (b) Simulated and experimental adsorption enthalpy for O₂ in Mg-MOF.

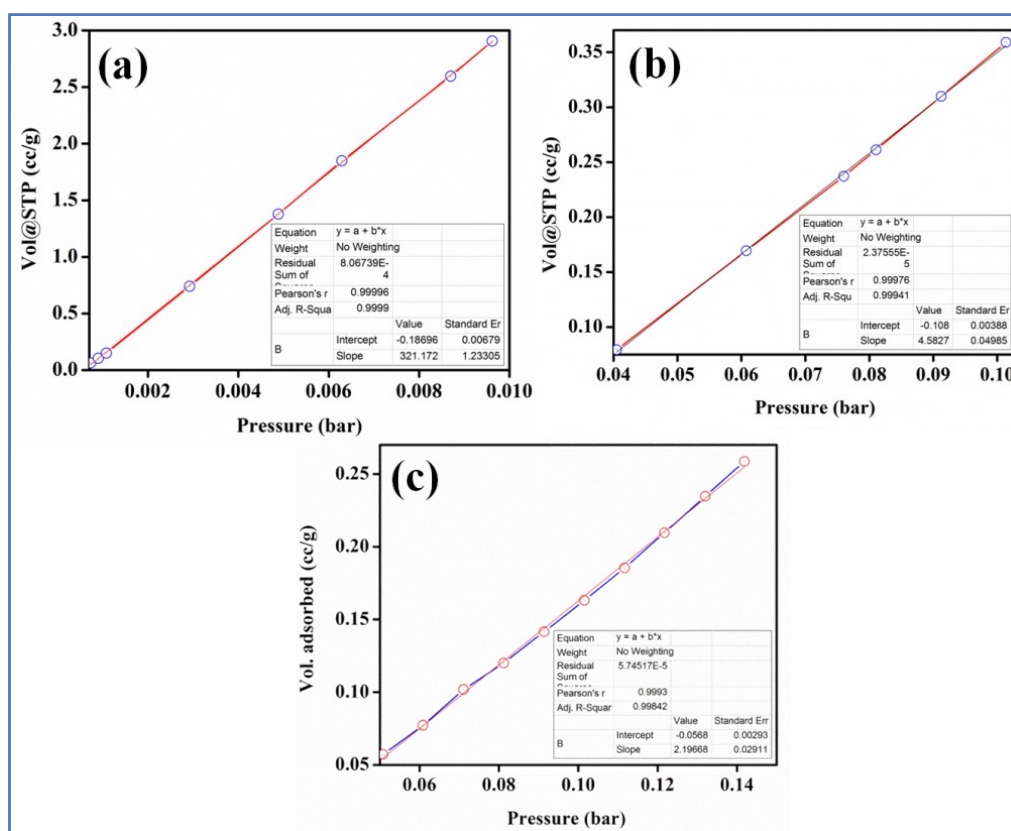


Figure S12. Calculation of gas selectivity constant for (a) CO₂ and (b) N₂ and (c) O₂ gases using on Henry law.

COMPUTATIONAL MODELLING PART

1. MICROSCOPIC MODELS FOR THE HOST FRAMEWORK

The experimentally elucidated structure of Mg-MOF was initially geometry optimized at the Density Functional Theory (DFT) level using the CP2K package.¹⁶ In these simulations, the positions of atoms in the framework were relaxed while the unit cell parameters were kept fixed at the values determined experimentally. All the structural optimizations were done using Perdew-Burke-Ernzerhof (PBE)^{17,18} functional along with a combined Gaussian basis set and pseudopotential. For Carbon, Nitrogen, Oxygen, and Hydrogen, a triple zeta (TZVP-MOLOPT) basis set was considered, while a double zeta (DZVP-MOLOPT) was applied for Magnesium.¹⁹ The pseudopotentials used for all of the atoms were those derived by Goedecker, Teter, and Hutter.²⁰ The van der Waals interactions were taken into account via the use of semi-empirical dispersion corrections as implemented in the DFT-D3 method.²¹ The atomic point charges for all framework atoms in Mg-MOF (Figure S13) were obtained using the REPEAT method proposed by Campana et al.,²² which was implemented into the CP2K code based on a restrained electrostatic potential framework.²³

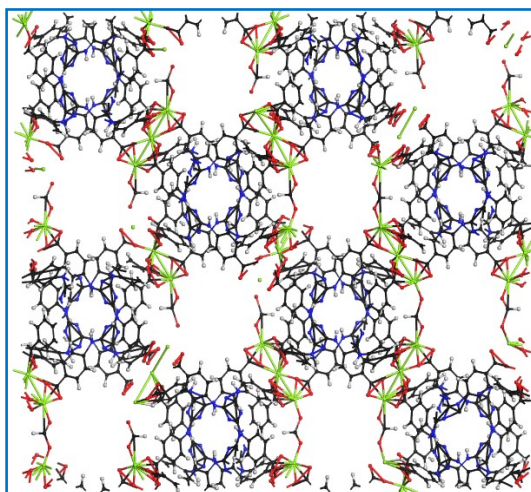


Figure S13. The single unit cell ($1\times 1\times 1$ simulation box) of Mg-MOF considered for the DFT calculations viewed along c -direction. (black, carbon; grey, hydrogen; red, oxygen; green, Magnesium).

2. DFT DERIVED

SPECIFIC FORCEFIELDS

The interaction between the guest molecules and Mg-MOF except for coordinatively unsaturated metal center (CUS), i.e. Mg, were explained by using the sum of a 12-6 Lennard-Jones (LJ) contribution and a columbic term. Due to the presence of CUS, we derived a specific forcefield to explain guest to host interactions. Here Buckingham analytic function with the aid of Density Functional Theory (DFT) based energy including Basis Set Superposition Error (BSSE) correction employed to address guest-host interaction (eqn 1).

$$U_{ij} = \underbrace{\sum_{i < j} \frac{1}{4\pi\epsilon_0} \frac{q_i q_j}{r_{ij}}}_{\text{Electrostatic term}} + \underbrace{4\epsilon_{ij} \left[\left(\frac{\sigma_{ij}}{r_{ij}} \right)^{12} - \left(\frac{\sigma_{ij}}{r_{ij}} \right)^6 \right]}_{\text{Lennard-Jones term}} + \underbrace{\left[A_{ij} e^{-B_{ij} r_{ij}} - S_g \frac{C_{ij}}{r_{ij}^6} \right]}_{\text{Buckingham term}} \dots\dots\dots 1$$

ϵ_{ij} and σ_{ij} indicate the interacting pair LJ parameter and the interaction parameters obtained through Lorentz-Berthelot mixing rules (i.e., a geometric combining rule for the energy and an arithmetic one for the atomic size: $\epsilon_{ij} = (\epsilon_i \epsilon_j)^{1/2}$ and $\sigma_{ij} = (\sigma_i + \sigma_j)/2$). The second term is the Columbic contribution between point charges q_i and q_j separated by a distance r_{ij} . A, B and C are the conventional Buckingham parameters for repulsive and attractive contribution, respectively and S_g indicates the global scaling factor for the dispersion energies.

For generating Buckingham potentials (A, B, and C parameters) from binding energy profile of guest-host interaction, we performed DFT calculation for the interaction of adsorbate molecules on a symmetric cluster of Mg-MOF framework having an unsaturated metal center (Figure S13) which interact directly with the metal center, Mg. The respective symmetric cluster was placed in a tetragonal simulation box having the composition of $\text{Mg}_3\text{C}_{50}\text{H}_{32}\text{N}_{18}\text{O}_{14}$ structural unit. Further, the binding energy of cluster to guest results in the potential energy curve and utilize to derive force field. All the energy calculations are performed with the help

of DFT-based CP2K Package¹⁶ and followed as same as the principles mentioned above. The binding energy was calculated as follows:

$$E_{B.E} = E_{(symmetrical\ unit + Guest)} - \{E_{(symmetrical\ unit)} + E_{(Guest)}\}$$

Where $E_{(symmetrical\ unit + Guest)}$, $E_{(symmetrical\ unit)}$ and $E_{(Guest)}$ indicate the energy of optimized symmetrical unit with adsorbate molecule, optimized symmetrical unit, and optimized guest molecule, respectively.

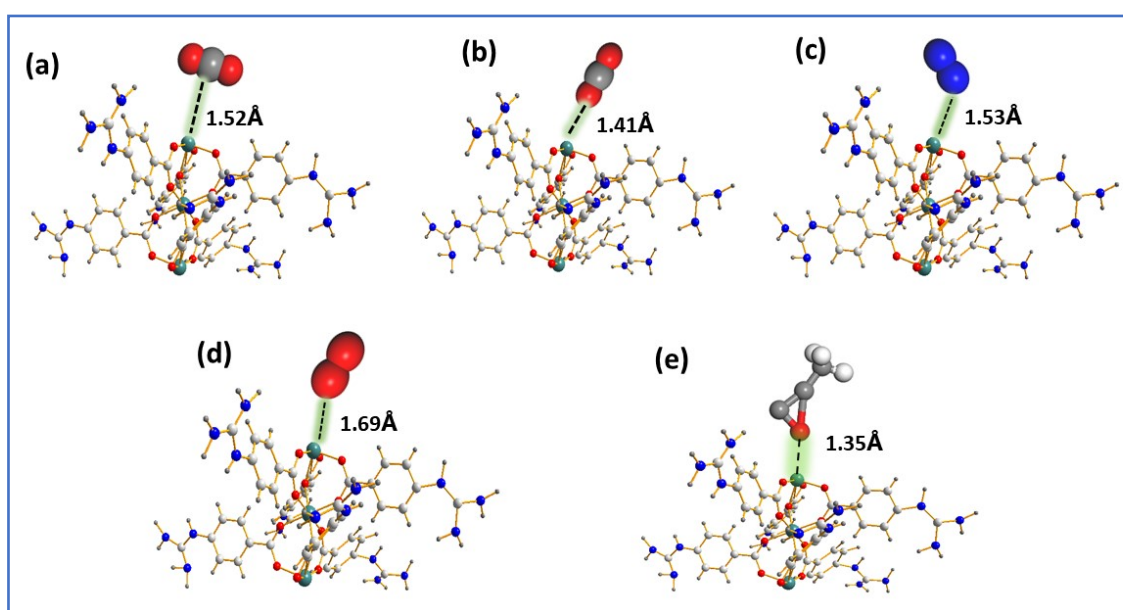


Figure S14. DFT geometry optimization of Mg-MOF cluster model with (a, b) CO₂, (c) N₂, (d) O₂ and (e) PO interaction to LA Mg(II) site.

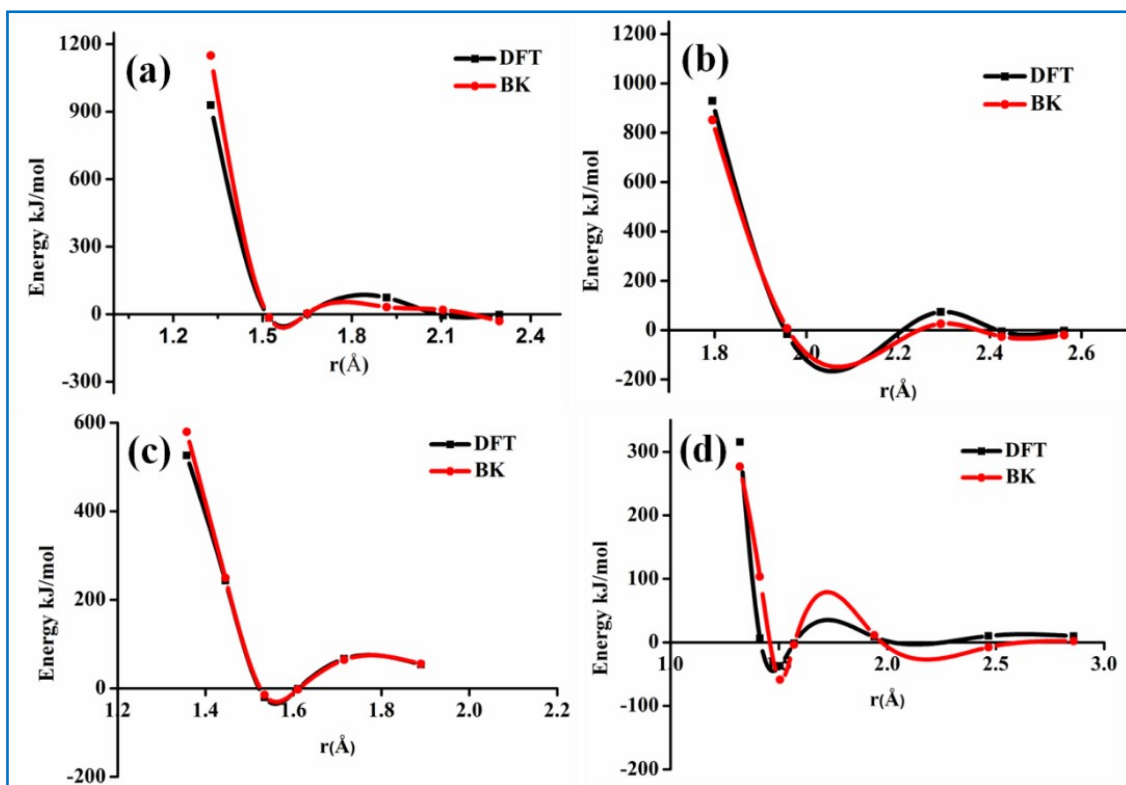
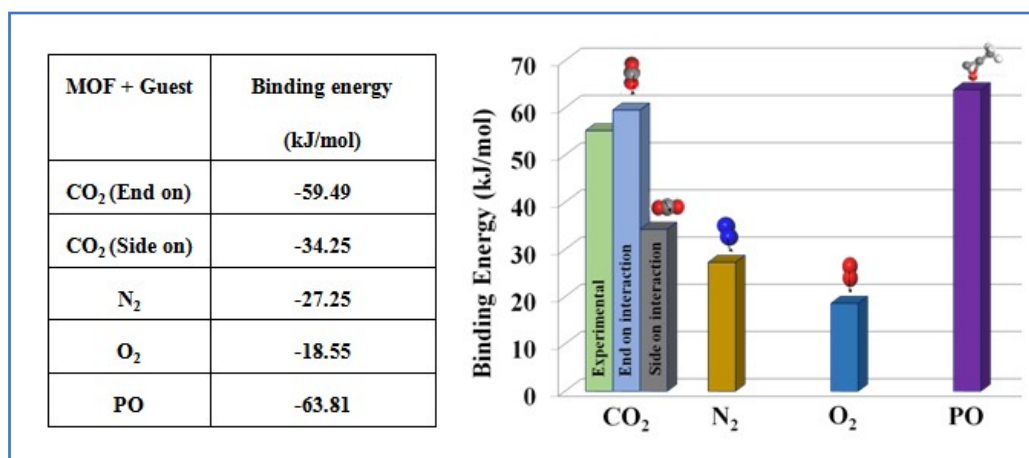


Figure S15. The potential energy values are calculated as moving each molecule along the dashed line, (a) CCO₂, (b) OCO₂, (c) NN₂, and (d) OO₂ (comparison of DFT-derived forcefield fitted curve (red circles) on the DFT interaction energy profile (black squares)).

Table S5. The DFT based binding energy calculated with PBE functional by Mg-MOF and Guest interaction.



The Universal force field (UFF) and DREIDING was adopted to describe the LJ parameters for the respective inorganic and organic part of the atoms in the MOF framework (Table S5).²⁴ In this work, CO₂ has been modeled as a rigid molecule through the EPM2 intermolecular potential²⁵ N₂ and O₂ as three site models, and its interaction potentials were taken from by TraPPE²⁶ (Table S6). The derived Buckingham parameters are listed below (Table S7).

Table S6. LJ potential parameters for the atoms of the Mg-MOF

Atomic type	DREIDING	
	σ (Å)	ϵ / k_B (K)
C	3.473	47.860
H	2.844	7.6490
O	3.033	48.158
N	3.662	34.724
Mg	2.6914	55.857

Table S7. Potential parameters and partial charges for the adsorbates.

Atomic type	σ (Å)	ε /k_B (K)	q (e)
CO ₂ _C	2.757	28.129	0.6512
CO ₂ _O	3.033	80.507	-0.3256
N ₂ _N	3.310	36.000	-0.4820
N ₂ _COM	0.000	0.000	0.9640
O ₂ _O	3.050	54.400	-0.1120

Table S8. Buckingham parameters associated with the Mg-MOF and adsorbates

Atomic type	A	B	C
C _{CO2} _Mg	3.5e6	8.5	2186.55
O _{CO2} _Mg	3.1e6	4.23	1000
N _{N2} _Mg	3.8e5	3.69	1000
O _{O2} _Mg	4.3e6	5.89	1000
O _{H2O} _Mg	8.9e5	4.09	738.13

3. GCMC Simulations

Grand Canonical Monte Carlo (GCMC) simulations were carried out at two different temperatures, 273 K and 298 K, for Mg-MOF to predict the single-component adsorption of CO₂, N₂, and O₂, and co-adsorption of wet air composition. These calculations were performed using the RASPA simulation code.²⁷ The simulation box was made of 2 (2×1×1) unit cells of Mg-MOF. Short-range dispersion forces were truncated at a cut off radius of 12 Å while the interactions between unlike force field centers *a* and *b* were treated utilizing the Lorentz-Berthelot combination rules; $\varepsilon_{ab} = \sqrt{\varepsilon_a \varepsilon_b}$, $\sigma_{ab} = (\sigma_a + \sigma_b)/2$, where ε_a and σ_a are the LJ parameters for the species *a*. The long-range electrostatic interactions were handled using the Ewald summation technique. The fugacities for each adsorbed species at a given thermodynamic condition were computed with the Peng-Robinson equation of state (EoS).²⁸ For each state point, 5×10⁷ Monte Carlo steps have been used for both equilibration and production runs. Three types of trials were considered for the molecules: (i) translation or rotation, (ii) creation/deletion, and (iii) exchange of molecular identity. The adsorption enthalpy at low coverage (Δh) for each gas was calculated through configurational-bias Monte Carlo simulations performed in the NVT ensemble using the revised Widom's test particle insertion method.²⁹ Additionally, to gain insight into the configurational distribution of the adsorbed species in Mg-MOF, some additional data were calculated at different pressure including the radial distribution functions (RDF) between the guests and the host.

The selectivity (S) for CO₂ over the combination of N₂ and O₂ was calculated by the following

expression: $S(\text{CO}_2/\text{N}_2+\text{O}_2) = \left(\frac{x_{\text{CO}_2}}{x_{\text{N}_2} + x_{\text{O}_2}}\right) \left(\frac{y_{\text{N}_2} + y_{\text{O}_2}}{y_{\text{CO}_2}}\right)$ where x_{CO_2} , x_{N_2} and x_{O_2} are the mole fractions of CO₂, N₂, and O₂ in the adsorbed phase, respectively, while y_{CO_2} , y_{N_2} and y_{O_2} are the mole fractions of CO₂, N₂, and O₂ in the bulk phase, respectively. Additionally, we

executed the selectivity for CO₂ over the combination of N₂ and O₂ with various range of humidity and bare CO₂ adsorption in maximum loaded water itself.

4. Computational Calculation on Catalysis

Periodic DFT calculations were carried out in the mixed Gaussian plane wave scheme as implemented in the CP2K package³⁰ with Grimme's D3 dispersion corrections.³¹ The PBE functional³² was used to calculate the exchange-correlation energy. For Carbon, Oxygen, Nitrogen, and Hydrogen, a triple zeta (TZVP-MOLOPT) basis set was considered, while a double zeta (DZVP-MOLOPT) was applied for Magnesium.³³ The pseudopotentials used for all of the atoms were those derived by Goedecker, Teter and Hutter.³⁴ This basis set and energy cut-off parameters have been considered based on the previous calculation by Ye *et al.*³⁵ where they validated that PBE functional with a plane wave cutoff energy of 500 Ry and suggested as the best option for exploring the catalytic mechanism involves MOF.

For constructing Mg-MOF catalyst model, the unit cell of Mg-MOF (Figure S36a) was taken from the experimentally elucidated Mg-MOF, however, the calculations were carried out on the primitive cell (Figure S36b) to save computational time. The lattice constants of the optimized primitive cell are $a = 34.5309$, $b = 26.5157$, $c = 25.1753$ Å, $\alpha = 83.7869$, $\beta = 49.7625$, $\gamma = 46.4507^\circ$ and correspond to the unit cell with $a = 16.9995$, $b = 47.394$, $c = 50.233$ Å, $\alpha = \beta = \gamma = 90^\circ$. We found that fully relaxing the geometry and cell parameters of Mg-MOF gave lattice constants that were almost identical to the relaxed Mg-MOF values. Furthermore, optimizing the structure with chemisorbed PO and/or CO₂ in Mg-MOF also perturbed the lattice constants and energies by a very minor amount. Therefore, we held the lattice constants fixed at the ground state Mg-MOF values for most calculations to save computational time. For the calculation, the total relative energy of the Mg-MOF (catalyst), CO₂, and PO (isolated reactants) were considered to zero energy and the optimized structures of reactant complexes are depicted in Scheme 2. In the case of each stage of catalytic reaction (e.g. IS, IC, TS, RC,

FC, etc.), the relative energies were computed with respect to the sum of the total energies of the corresponding gas-phase molecules as represented in Equation 1.

$$E_{relative} = E_{stage} - (E_{MgMOF} - E_{CO_2} - E_{PO}) \quad (1)$$

Where E_{stage} , E_{MgMOF} , E_{CO_2} and E_{PO} represents the total energies of the Mg-MOF with adsorbates at each reaction stage, the empty Mg-MOF, gas-phase CO_2 and PO, respectively. Equation 1 defines negative values as exothermic and positive values as endothermic processes. Transition states along the reaction pathway were determined by using the climbing image nudged elastic band (CI-NEB) method. Transition states were confirmed through frequency analysis, verifying that the transition complex had only one imaginary frequency vibrational mode.

3.1. Computational predictions—single adsorption isotherm

RADIAL DISTRIBUTION FUNCTION

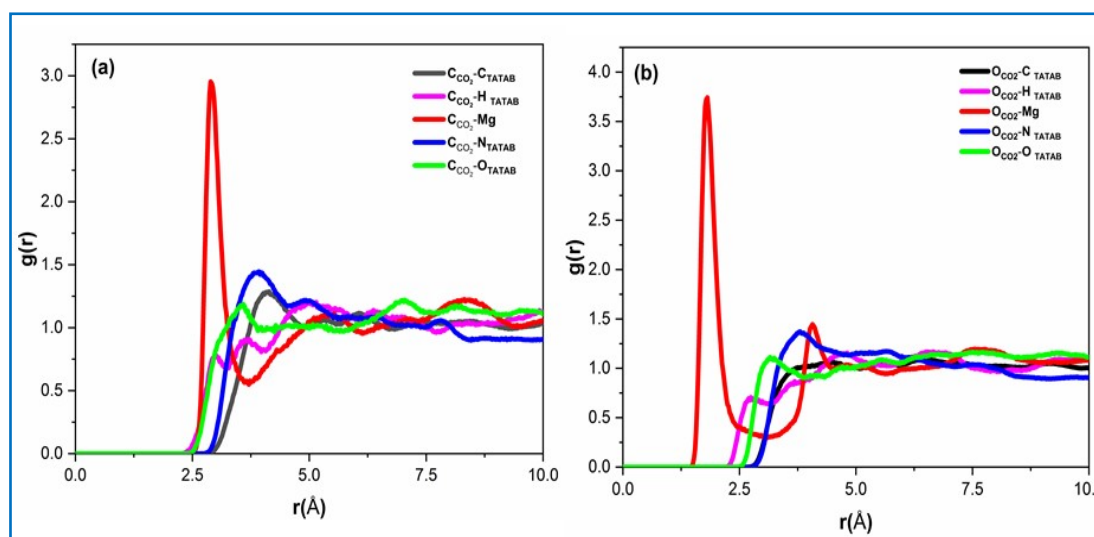


Figure S16. Radial distribution functions (RDF) between CO_2 and the atoms of the MOF framework (Organic nitrogen, N_{TATAB} : blue, Organic hydrogen, H_{TATAB} : Magenta and Organic

Oxygen, O_{TATAB} : green, Organic carbon, C_{TATAB} : black, Magnesium, Mg: red) extracted from the single component adsorption in Mg-MOF in 0.01bar at 273K.

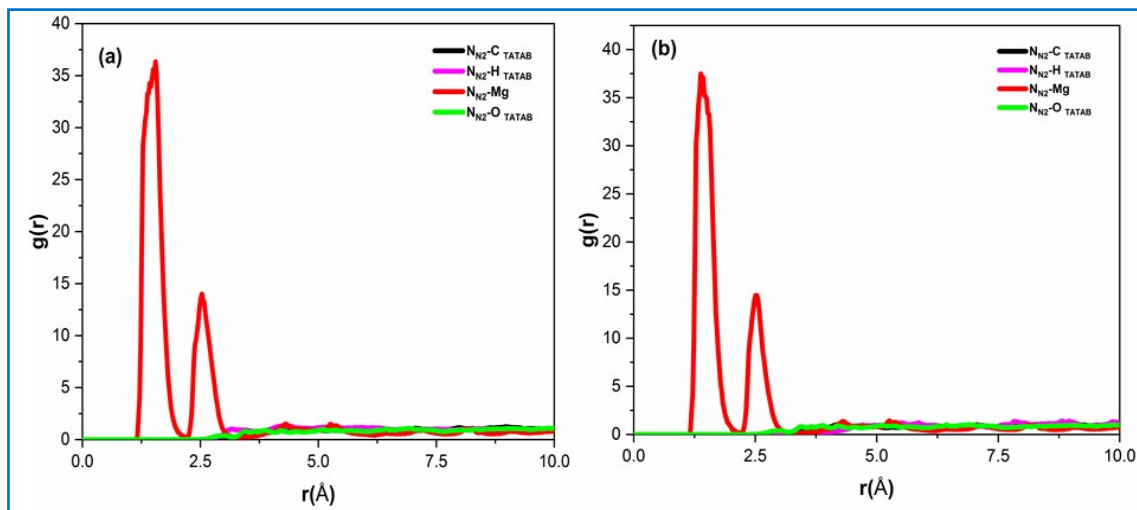


Figure S17. Radial distribution functions (RDF) between N_2 and the atoms of the MOF framework (Organic nitrogen, N_{TATAB} : blue, Organic hydrogen, H_{TATAB} : Magenta and Organic Oxygen, O_{TATAB} : green, Organic carbon, C_{TATAB} : black, Magnesium, Mg: red) extracted from the single-component adsorption in Mg-MOF in 0.01bar at 273K (a) and 298K (b).

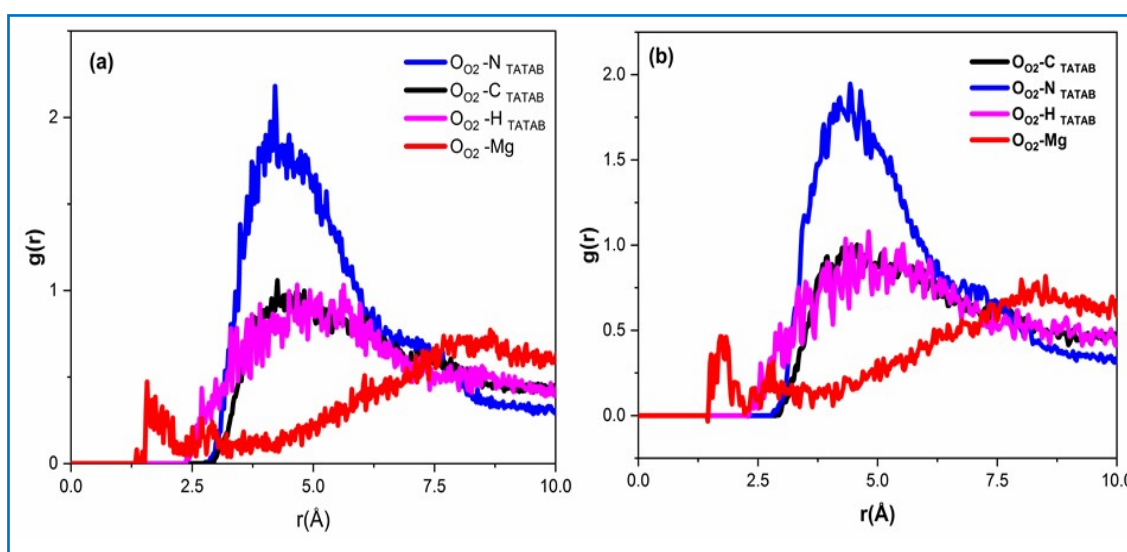


Figure S18. Radial distribution functions (RDF) between O₂ and the atoms of the MOF framework (Organic nitrogen, N_{TATAB}: blue, Organic hydrogen, H_{TATAB}: Magenta and Organic Oxygen, O_{TATAB}: green, Organic carbon, C_{TATAB}: black, Magnesium, Mg: red) extracted from the single component adsorption in Mg-MOF in 0.01bar at 298K.

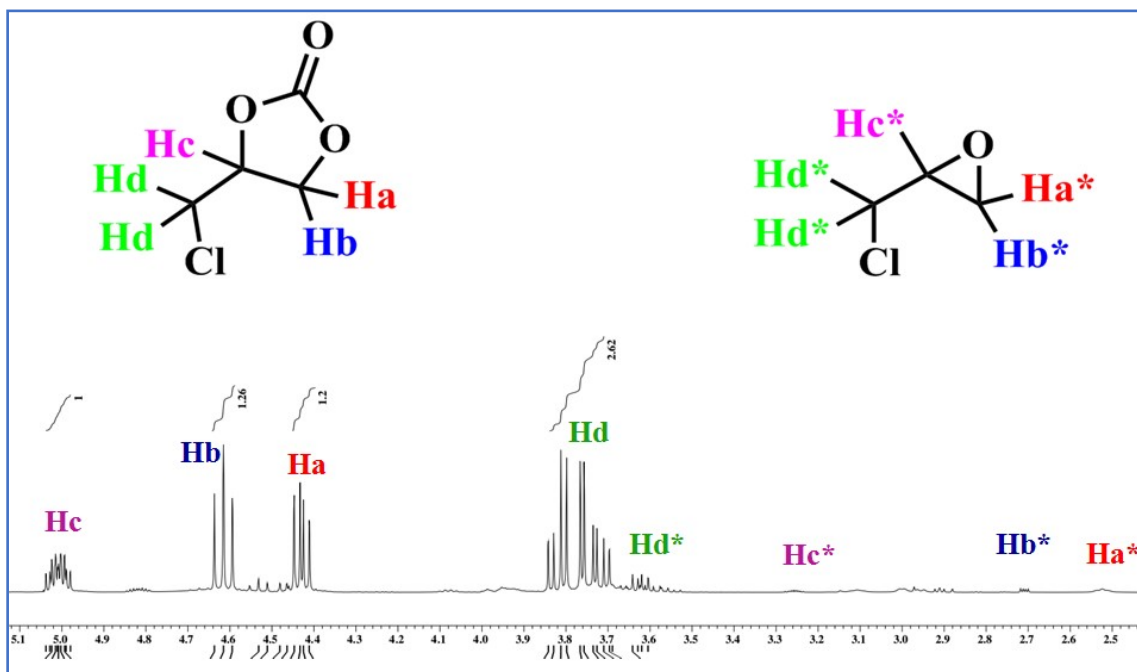


Figure S19. ¹H NMR (CDCl₃, 400 MHz) spectra for the cycloaddition reaction of epichlorohydrin (ECH) with CO₂ using Mg-MOF as catalyst.

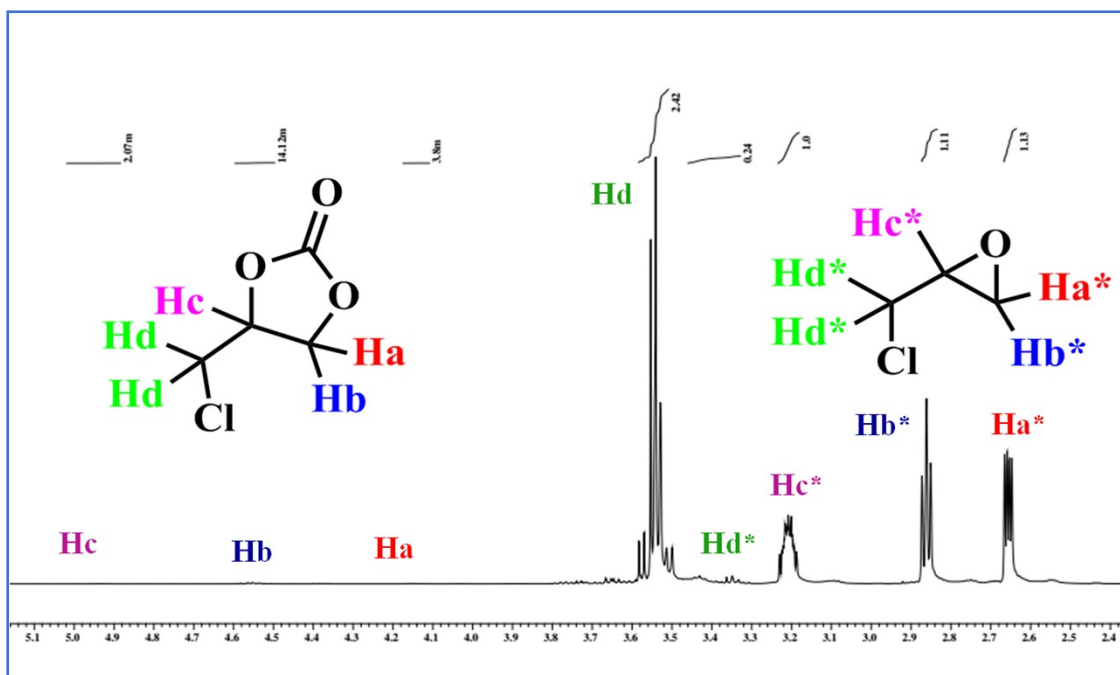


Figure S20. ^1H NMR (CDCl_3 , 400 MHz) spectra for the cycloaddition reaction of epichlorohydrin (ECH) with CO_2 using $\text{Mg}(\text{NO}_3)_2 \cdot 6\text{H}_2\text{O}$ metal salt as catalyst.

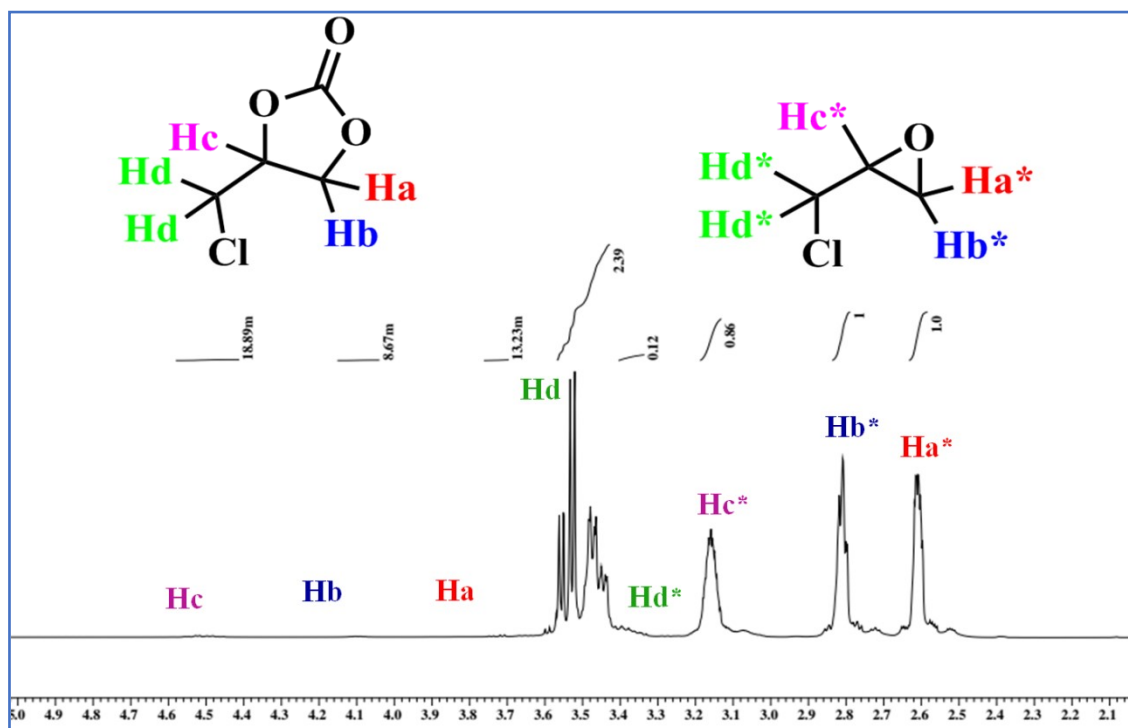


Figure S21. ^1H NMR (CDCl_3 , 400 MHz) spectra for the cycloaddition reaction of epichlorohydrin (ECH) with CO_2 using H_3TATAB ligand as catalyst.

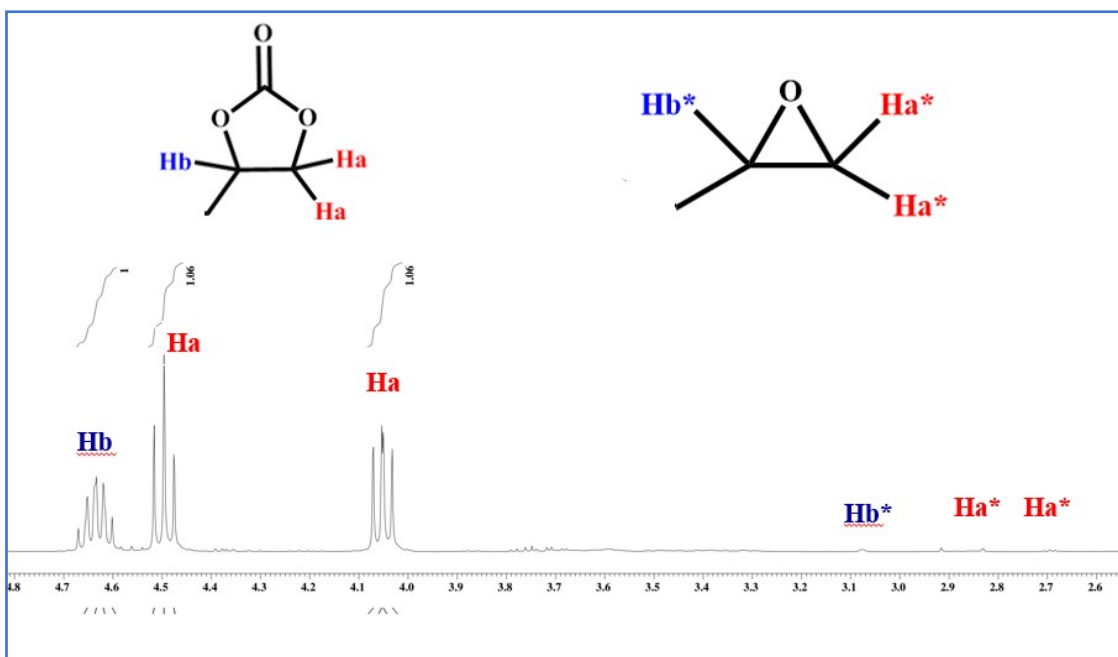


Figure S22. ^1H NMR (CDCl₃, 400 MHz) spectra for the cycloaddition reaction of 1,2-epoxypropane with CO₂ using Mg-MOF as the catalyst.

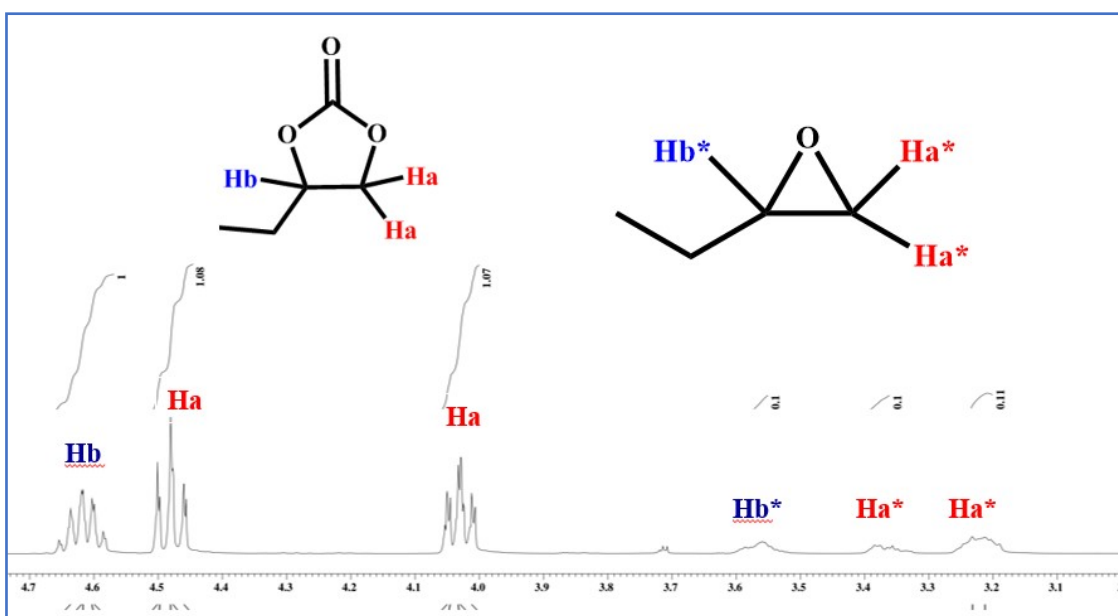


Figure S23. ^1H NMR (CDCl₃, 400 MHz) spectra for the cycloaddition reaction of 1,2-epoxybutane with CO₂ using Mg-MOF as catalyst.

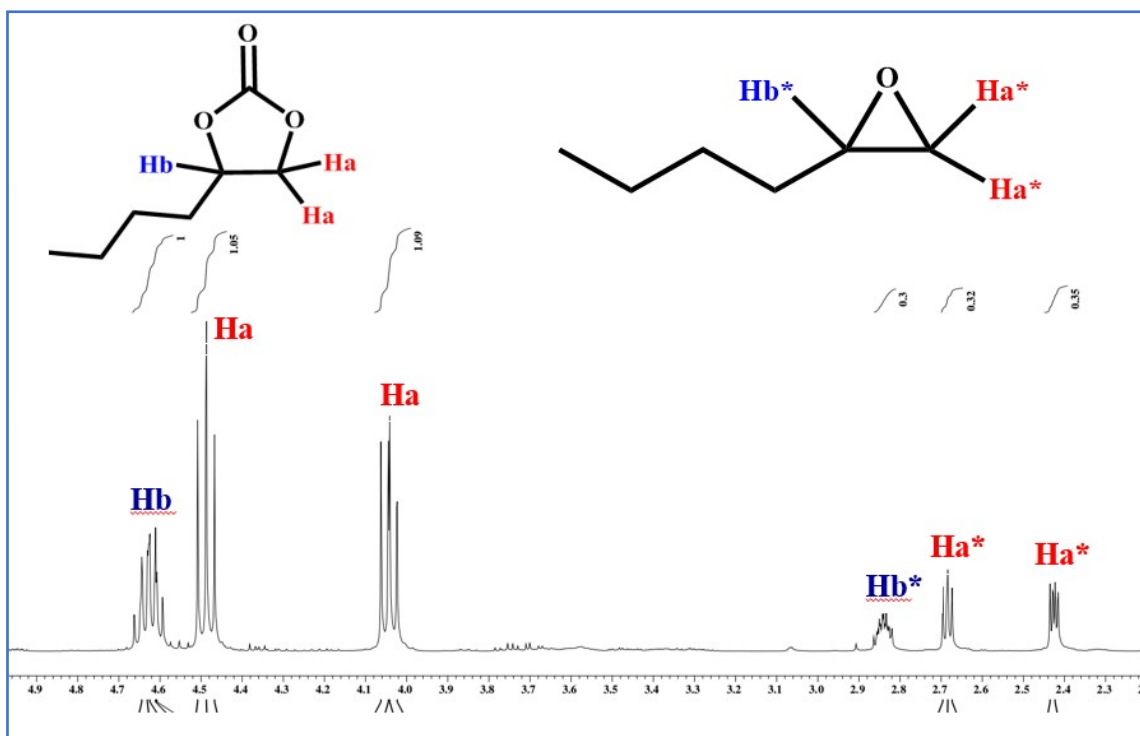


Figure S24. ^1H NMR (CDCl_3 , 400 MHz) spectra for the cycloaddition reaction of 1,2-epoxyhexane with CO_2 using Mg-MOF as catalyst.

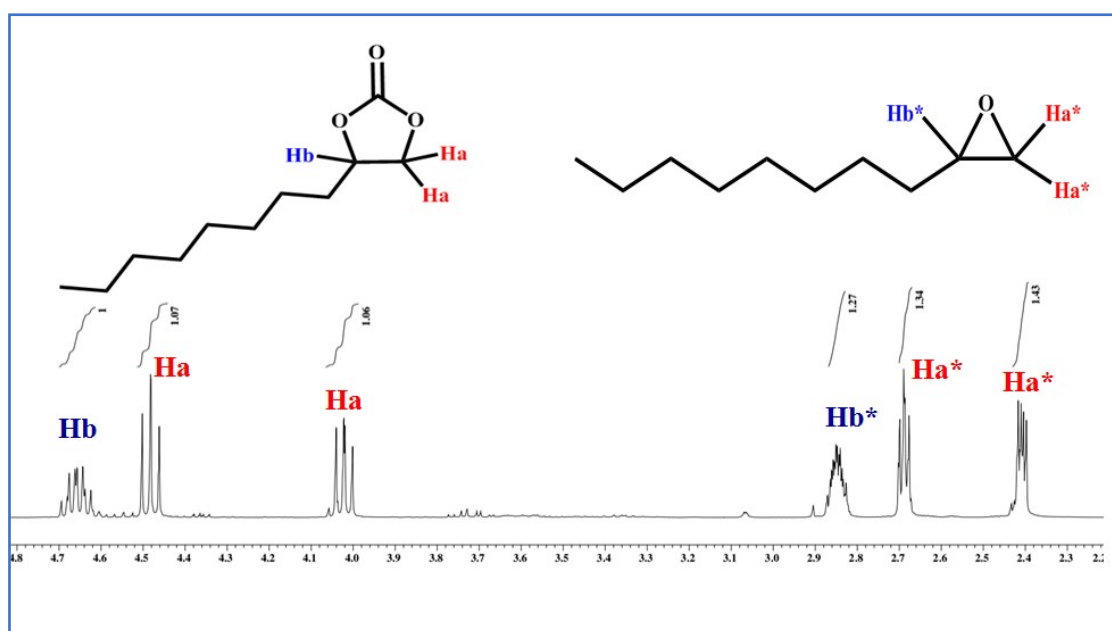
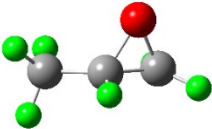
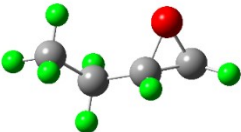
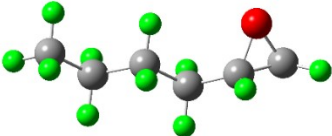


Figure S25. ^1H NMR (CDCl_3 , 400 MHz) spectra for the cycloaddition reaction of 1,2-epoxydecane with CO_2 using Mg-MOF as catalyst.

Table S9. Optimized geometries of epoxides using Gaussian09³⁶ at b3lyp/6-311g (d,p) level.

Substrates	Optimized structure	Dimensions
1,2-epoxy propane		4.35 X 3.41 Å ²
1,2-epoxy butane		5.648 X 3.39 Å ²
1,2-epoxy hexane		8.198 X 3.39 Å ²

1,2-epoxy decane		13.321 X 3.39 Å ²
allyl glycidyl ether		~8.901 X 3.140 Å ²
butyl glycidyl ether		~ 10.46 X 3.14 Å ²

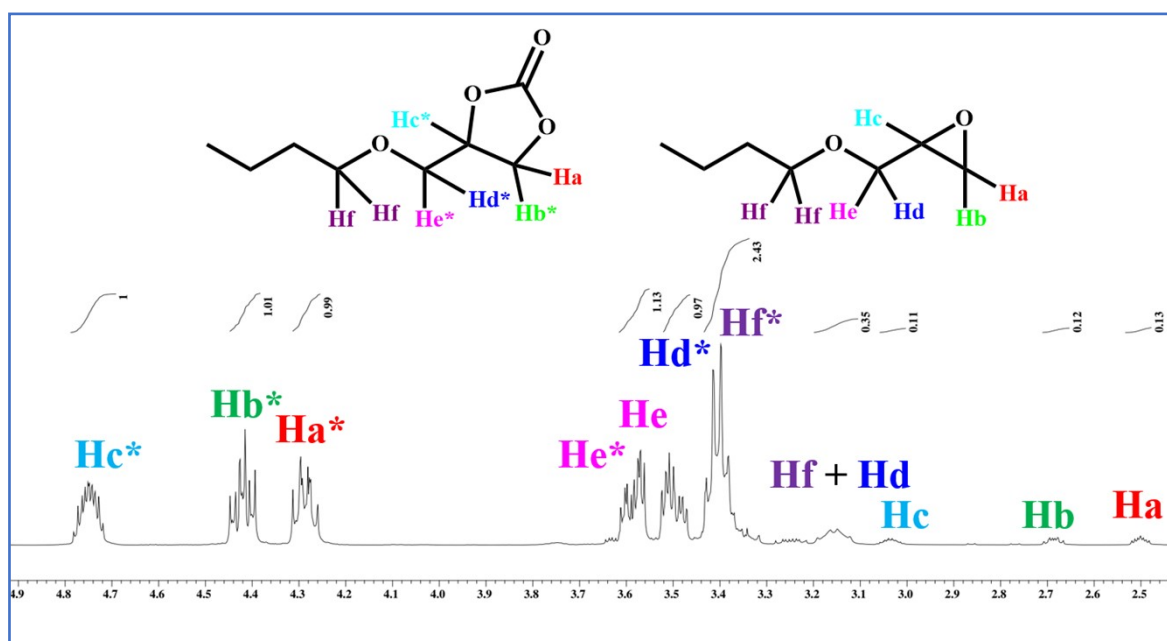


Figure S26. ¹H NMR (CDCl₃, 400 MHz) spectra for the cycloaddition reaction of butyl glycidyl ether with CO₂ using Mg-MOF as catalyst.

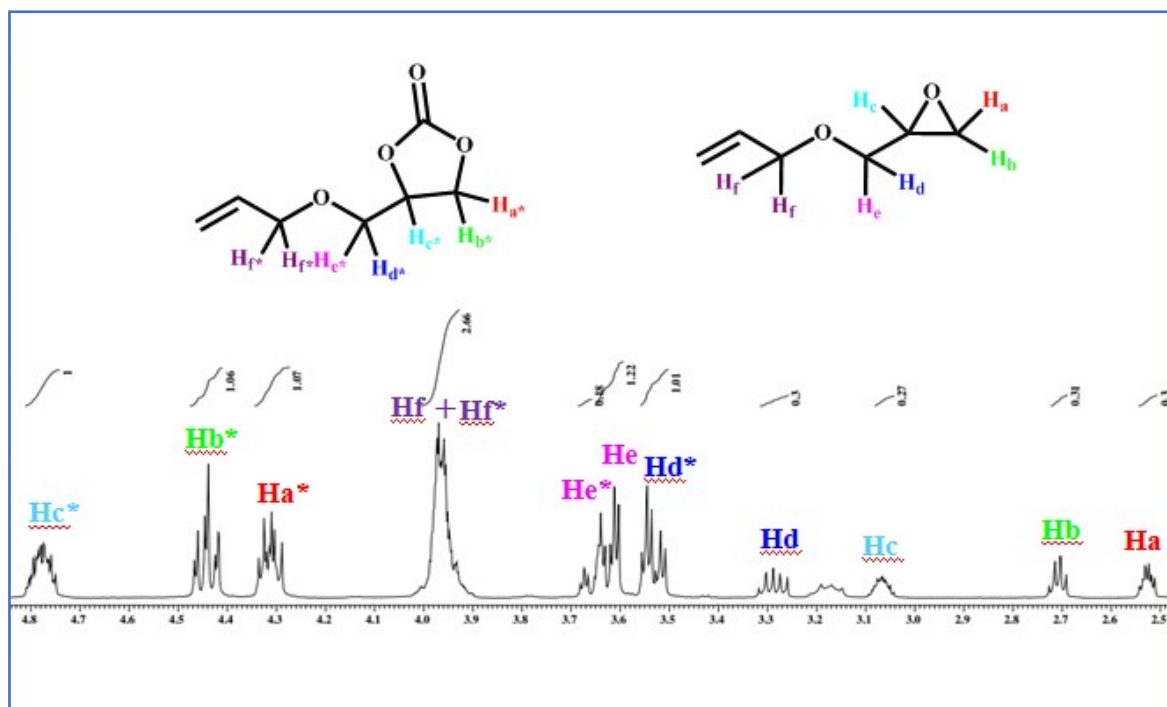


Figure S27. ^1H NMR (CDCl₃, 400 MHz) spectra for the cycloaddition reaction of allyl glycidyl ether with CO₂ using Mg-MOF as catalyst.

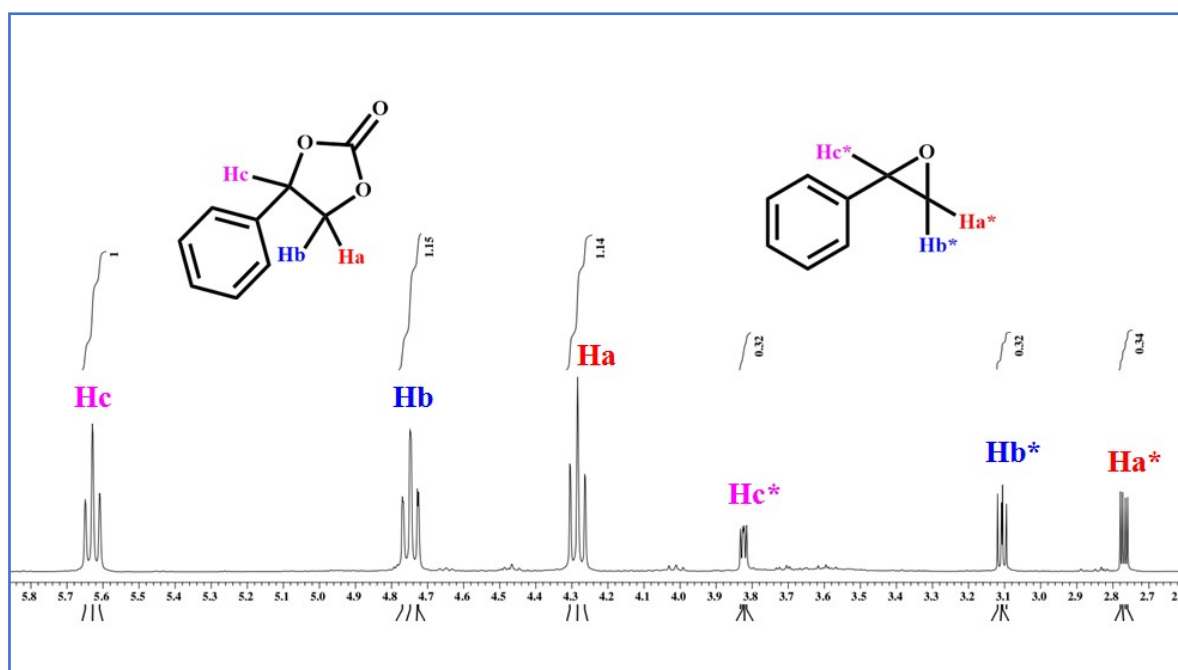


Figure S28. ^1H NMR (CDCl₃, 400 MHz) spectra for the cycloaddition reaction of styrene oxide with CO₂ using Mg-MOF as catalyst.

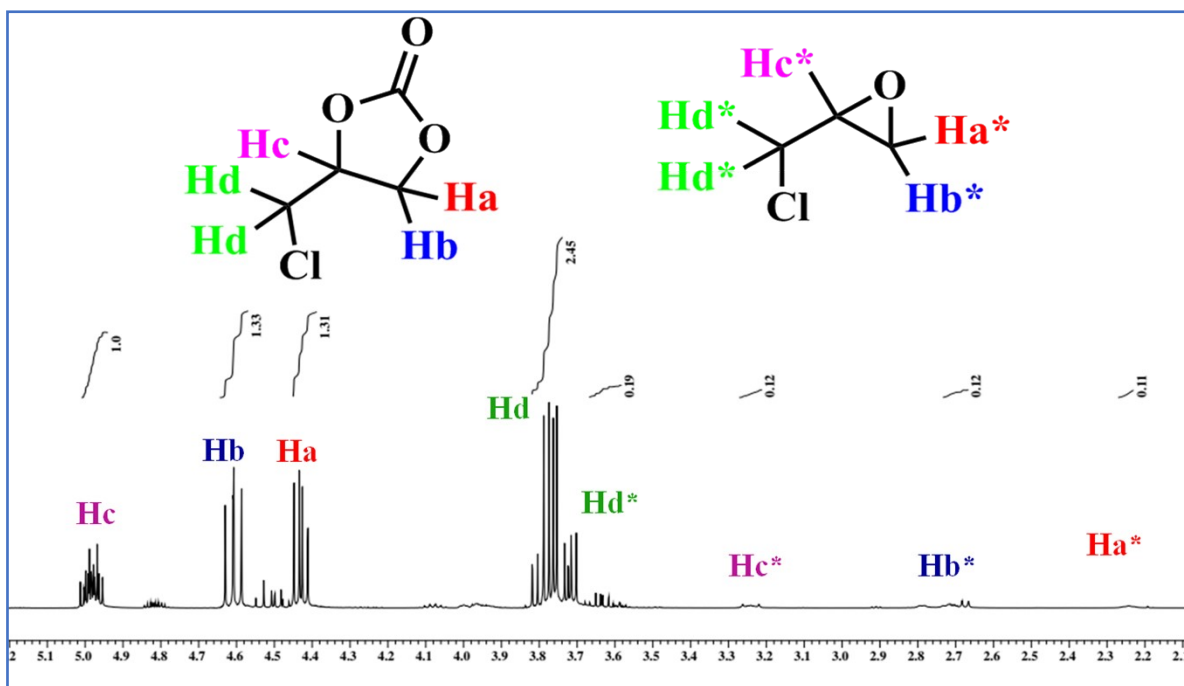


Figure S29. ^1H NMR (CDCl₃, 400 MHz) spectra for the cycloaddition reaction of ECH with simulated dry flue gas, CO₂:N₂ (13: 87%) using Mg-MOF as catalyst.

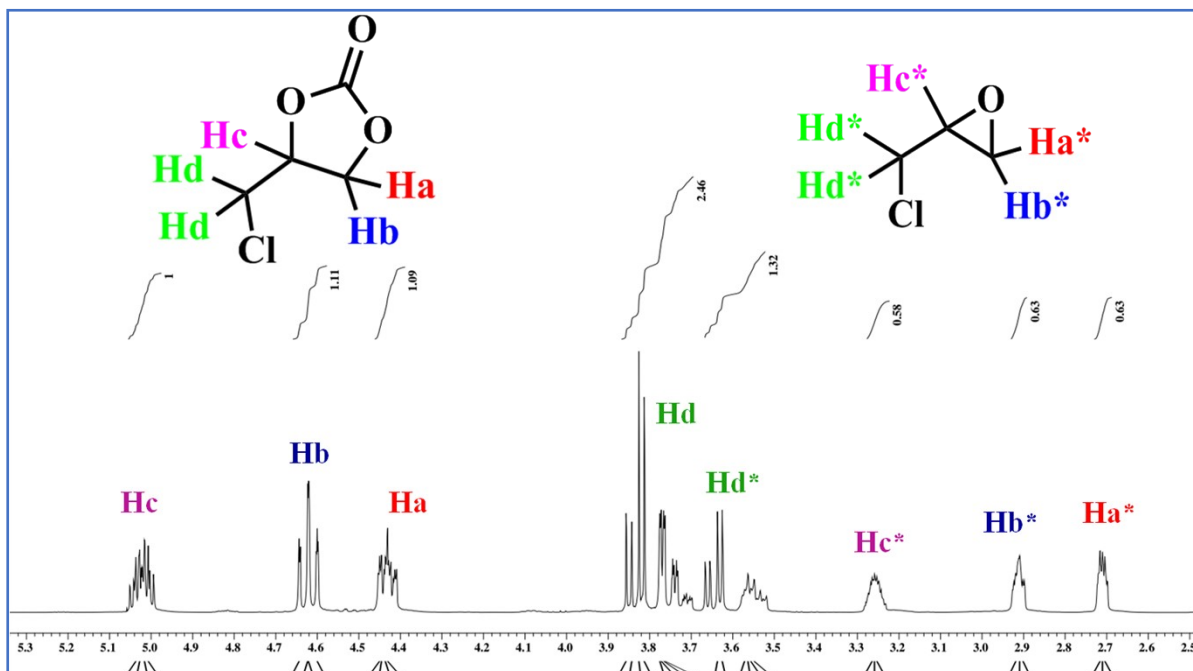


Figure S30. ^1H NMR (CDCl₃, 400 MHz) spectra for the cycloaddition reaction of ECH with CO₂ using direct air for 24 h.

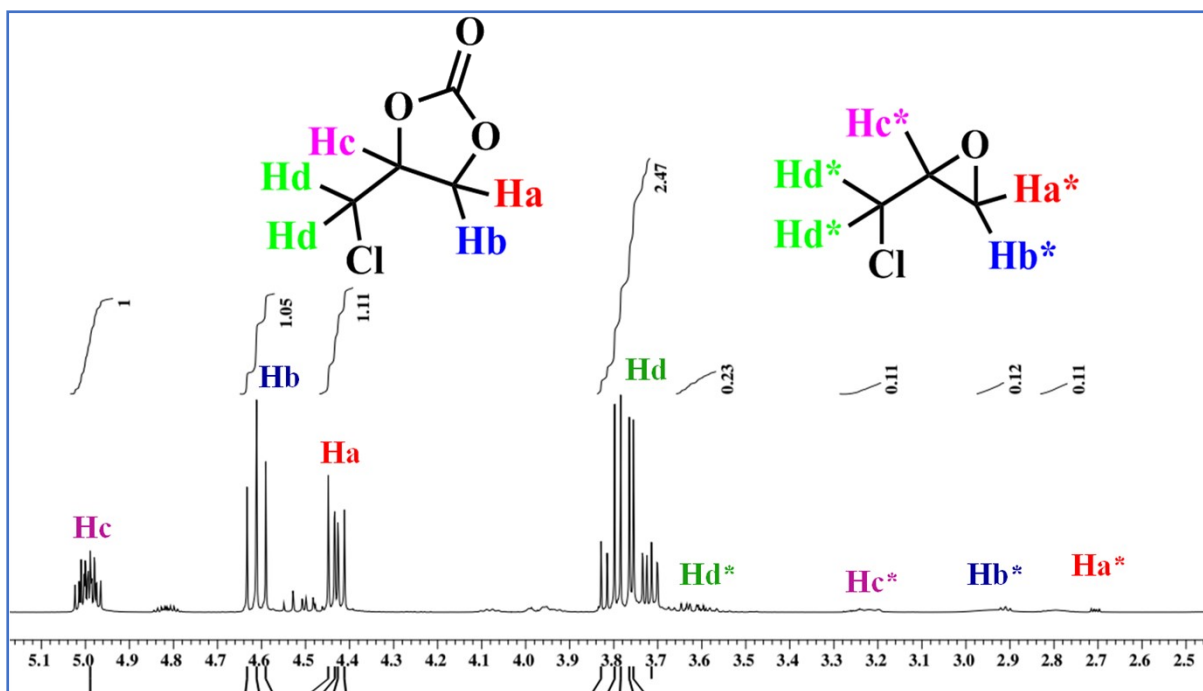
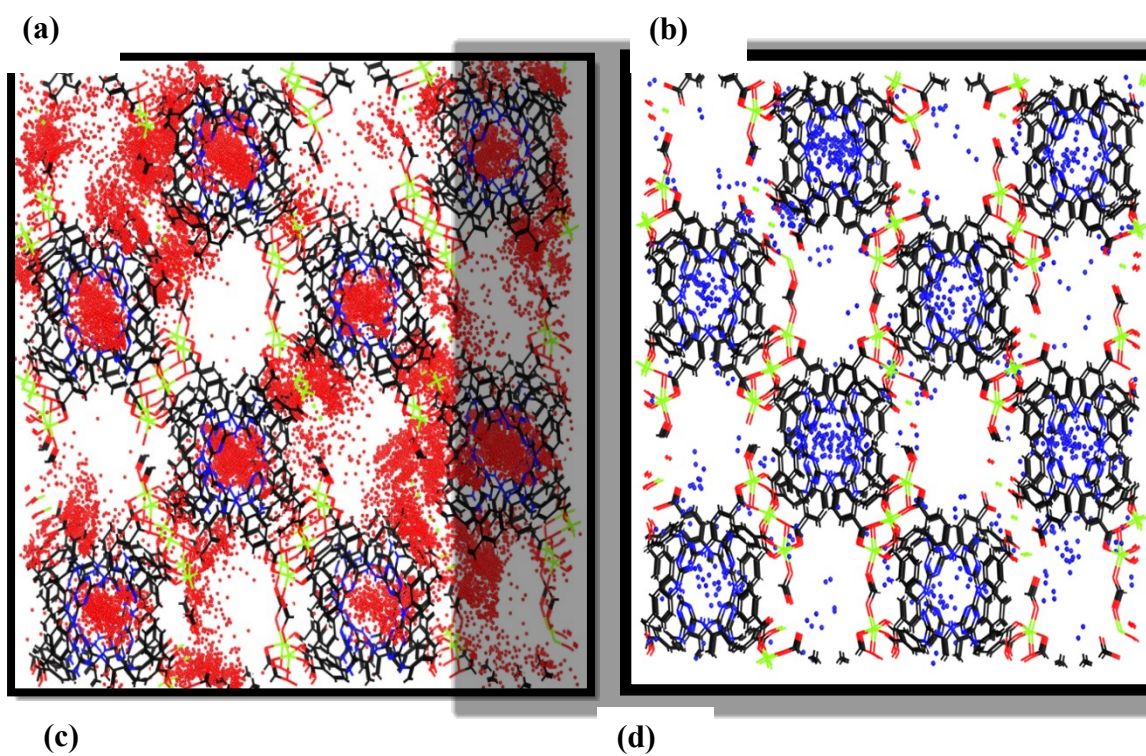


Figure S31. ^1H NMR (CDCl₃, 400 MHz) spectra for the cycloaddition reaction of ECH with CO₂ using direct air for 48 h.



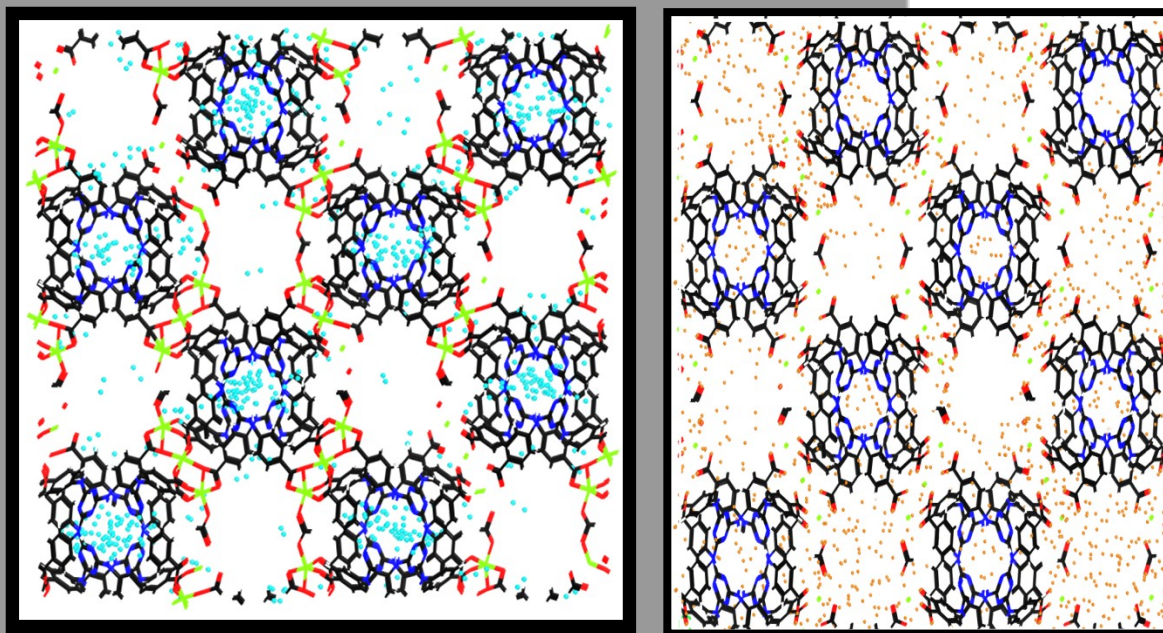


Figure S32. Maps of the occupied positions of CO₂ (a), N₂ (b) O₂ (c), and (d) H₂O in 500 equilibrated frames for a given pressure of 1 bar and at 298 K for Mg-MOF, color code for the atoms: C (black), Mg(green), O (red), H (grey), N(blue).

3.2 SELECTIVITY

CO₂/(N₂ + O₂)

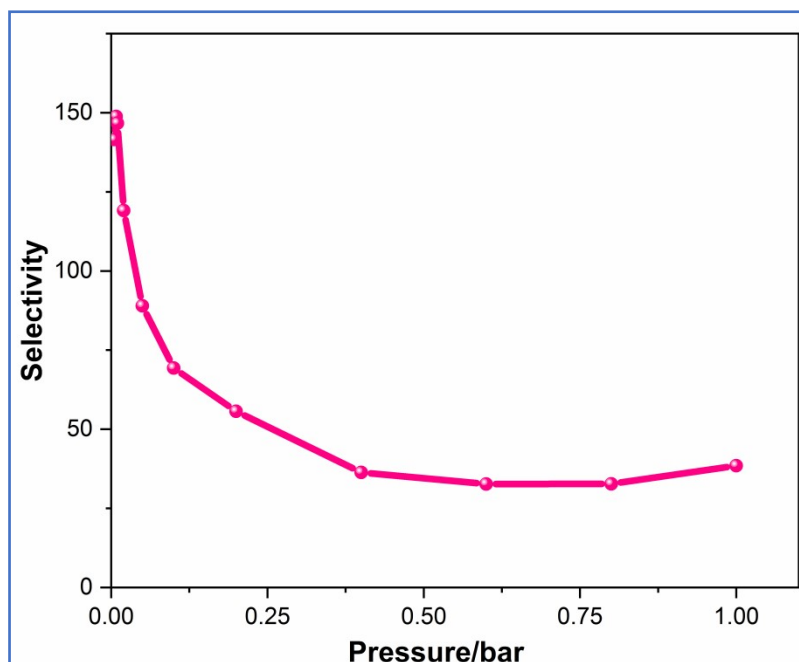


Figure S33. Selectivity plot of CO₂/(O₂ + N₂) in presence of RH = 1.57% at 298 K.

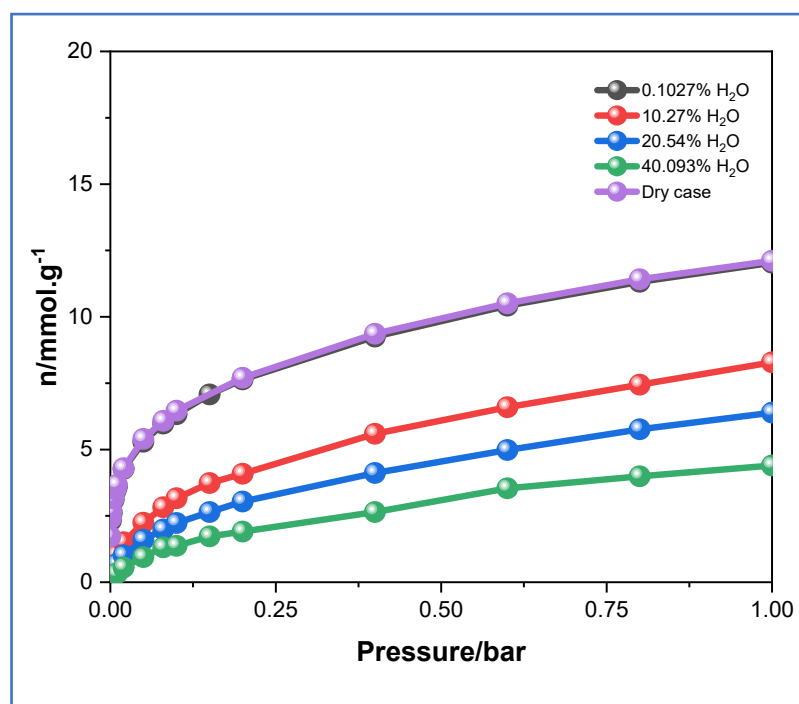


Figure S34. CO₂ adsorption isotherms at various relative humidity of pre-humidified Mg-MOF at 298K.

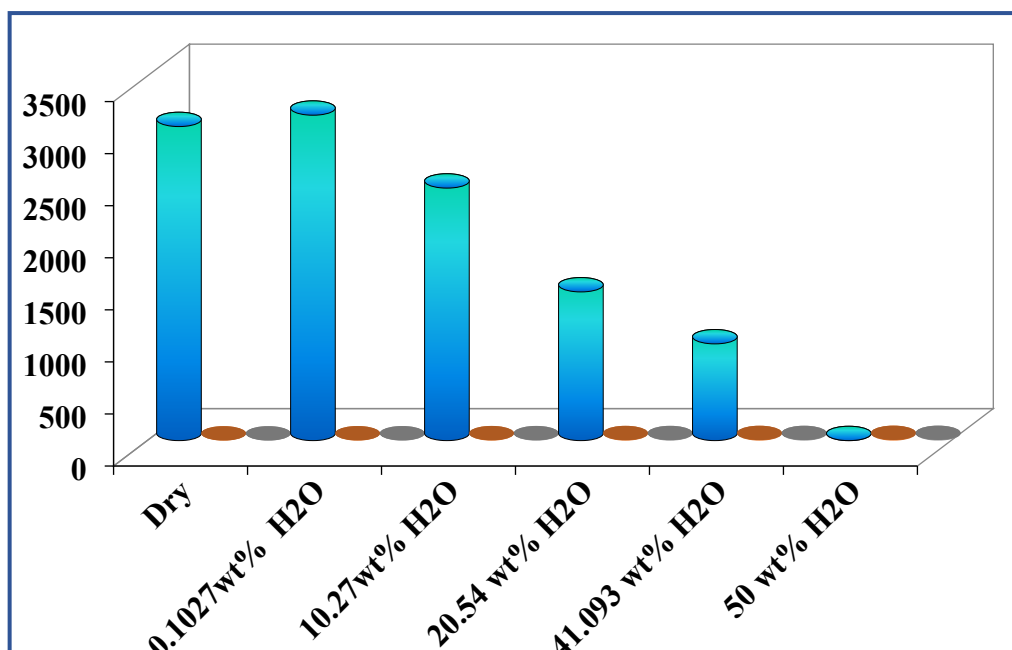


Figure S35. Simulated selectivity of CO₂/(O₂ + N₂) in various pre-humidified air at 1 bar.

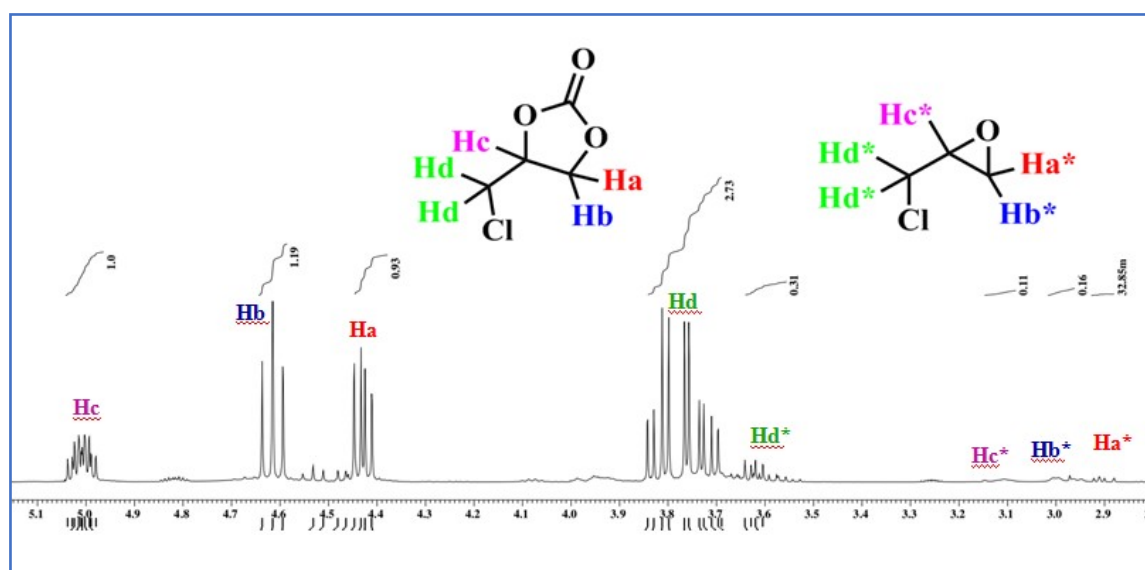


Figure S36. ¹H NMR (CDCl₃, 400 MHz) spectra for the cycloaddition reaction of ECH with CO₂ using Mg-MOF recycled after ten cycles of catalysis.

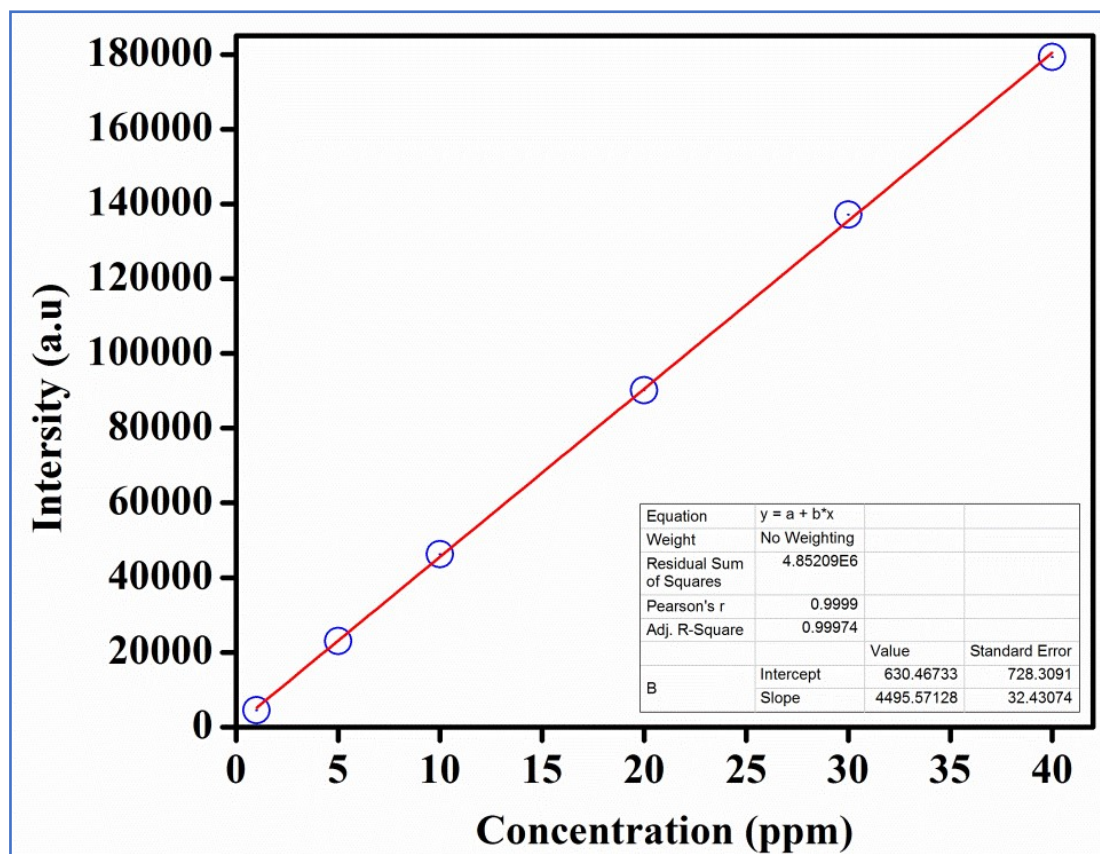


Figure S37. MP-AES calibration curve.

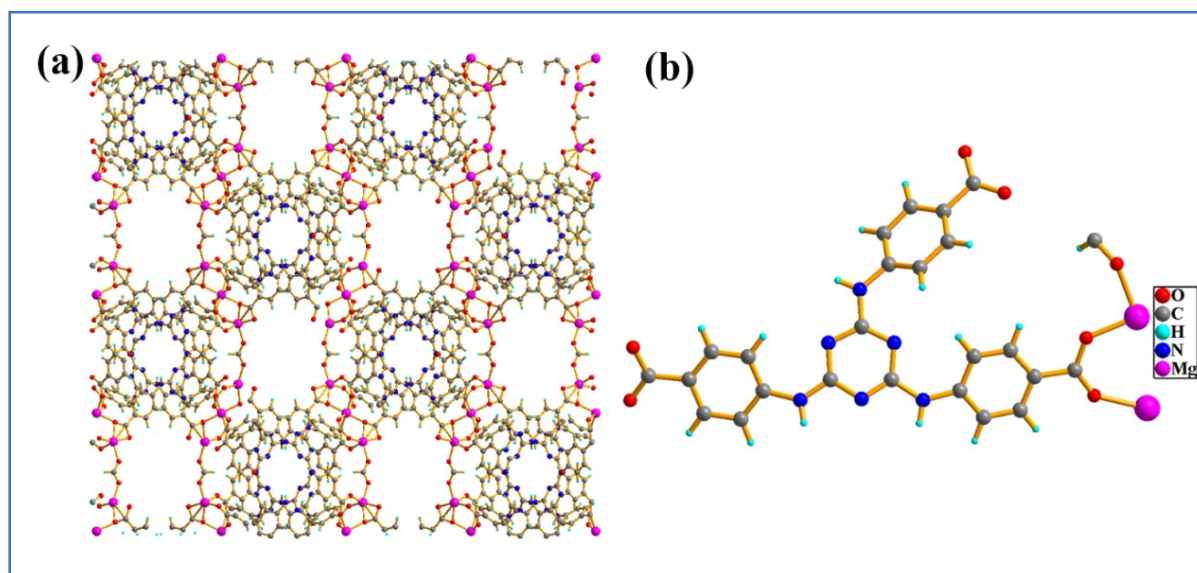


Figure S38. Unit crystal (left) and primitive (right) structure of Mg-MOF obtained through optimization via DFT method viewed along *a* vector direction.

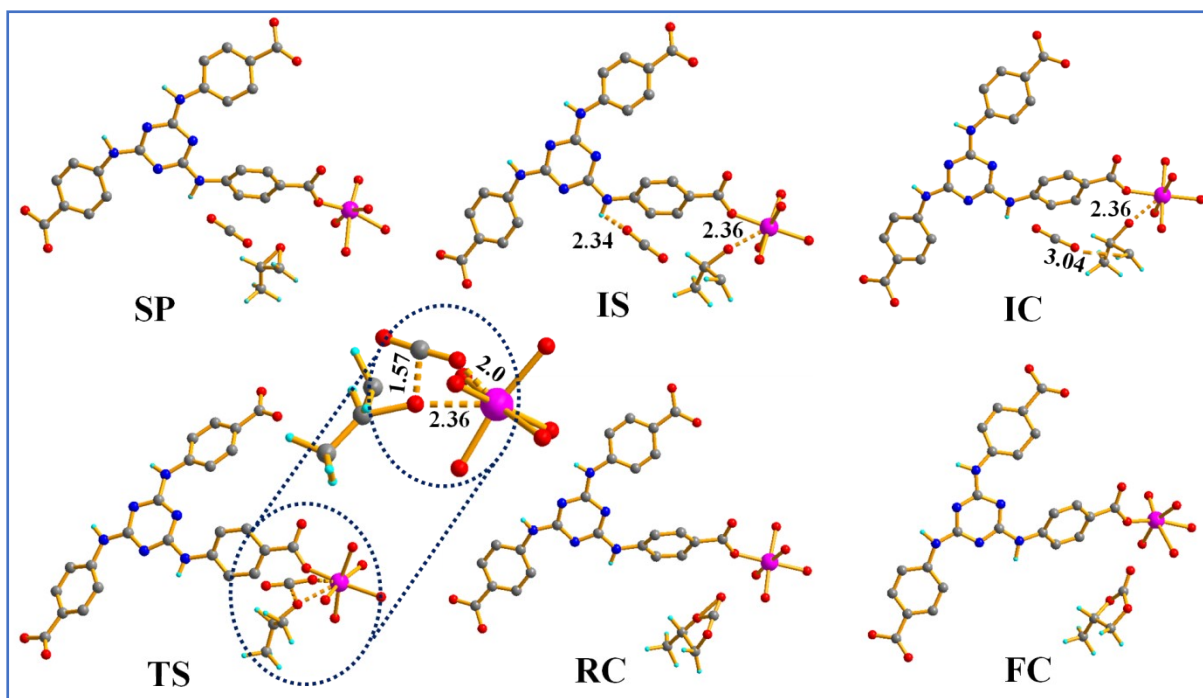


Figure S39. Mechanistic Pathways of the Intermediates and Transition States in the cycloaddition of propylene oxide and CO₂ using the Mg-MOF catalyst (bond distances are in Å).

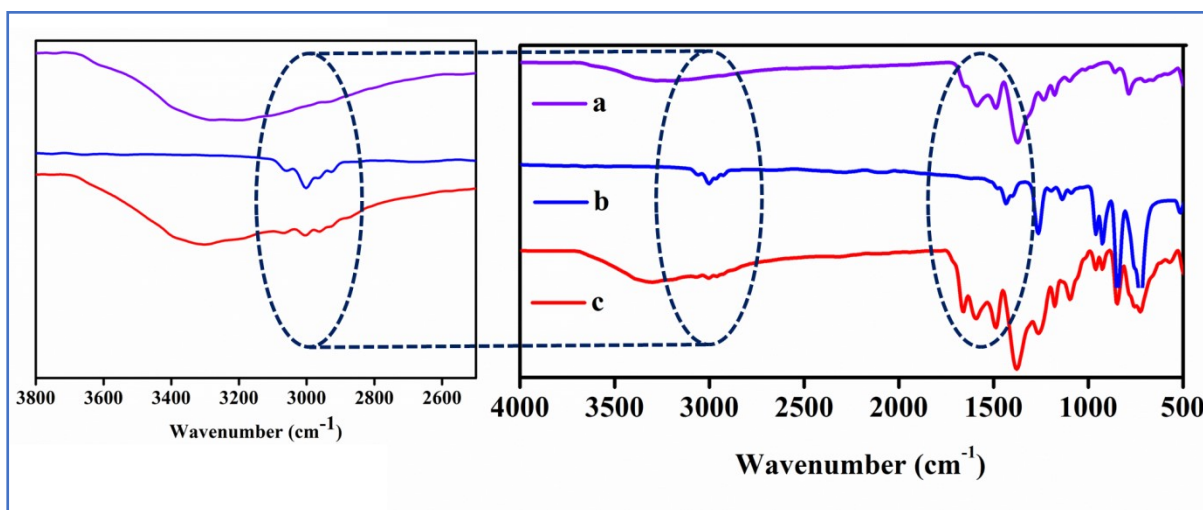


Figure S40. FT-IR spectra of (a) Mg-MOF, (b) Epichlorohydrin, and (c) Mg-MOF treated with epichlorohydrin.

References

- (1) W. Karuehanon, W. Fanfuenha, A. Rujiwatra and M. Pattarawarapan, Microwave-assisted SNAr reaction of 2,4,6-trichloro-1,3,5-triazine for therapid synthesis of C3-symmetrical polycarboxylate ligands, *Tetrahedron Lett.*, 2012, **53**, 3486-3489.
- (2) *SMART (V 5.628)*, *SAINT (V 6.45a)*, *XPREP*, *SHELXTL*; Bruker AXS Inc., Madison, Wisconsin, USA, **2004**.
- (3) G. M. Sheldrick, Siemens Area Detector Absorption Correction Program, University of Göttingen, Göttingen, Germany, **2004**.
- (4) A. Altomare, G. Cascarano, C. Giacovazzo and A. Guagliardi, Completion and refinement of crystal structures with *SIR92*, *J. Appl. Cryst.*, 1993, **26**, 343-350.
- (5) G. M. Sheldrick, *SHELXL-2014*, Program for Crystal Structure Solution and Refinement; University of Göttingen, Göttingen, Germany, **2014**.
- (6) L. J. Farrugia, WinGX-A Windows Programfor Crystal Structure Analysis, *J. Appl. Cryst.*, 2001, **45**, 849-854.
- (7) A. L. Spek, *J. Appl. Crystallogr.*, 2003, **36**, 7-13.
- (8) H. Pan, J. A. Ritter and P. B. Balbuena, Examination of the Approximations Used in Determining the Isothermic Heat of Adsorption from the Clausius–Clapeyron Equation, *Langmuir*, 1998, **14**, 6323–6327.
- (9) R. T. Yang, *Gas Separation by Adsorption Processes*, Butterworth, Boston, **1997**.
- (10) D. –A. Yang, H. –Y. Cho, J. Kim, S. –T. Yang and W. –S. Ahn, CO₂ capture and conversion using Mg-MOF-74 prepared by a sonochemical method, *Energy Environ. Sci.*, 2012, **5**, 6465–6473.
- (11) Y. B. N. Tran, P. T. K. Nguyen, Q. T. L. Khoi and D. Nguyen, Series of M-MOF-184 (M = Mg, Co, Ni, Zn, Cu, Fe) Metal-Organic Frameworks for Catalysis Cycloaddition of CO₂, *Inorg. Chem.*, 2020, **59**, 16747-16759.

-
- (12) H. Kim, M. Sohail, K. Yim, Y. C. Park, D. H. Chun, H. J. Kim, O. S. Han and J. –H. Moon, Effective CO₂ and CO Separation Using [M₂(DOBDC)] (M = Mg, Co, Ni) with Unsaturated Metal Sites and Excavation of Their Adsorption Sites, *ACS Appl. Mater. Interfaces*, 2019, **11**, 7014-702.
- (13) P. T. K. Nguyen, H. T. D. Nguyen, H. Q. Pham, J. Kim, K. E. Cordova and H. Furukawa, Synthesis and Selective CO₂ Capture Properties of a Series of Hexatopic Linker-Based Metal–Organic Frameworks, *Inorg. Chem.*, 2015, **54**, 10065–10072.
- (14) P. D. C. Dietzel, V. Besikiotis and R. Blom, Application of MetalOrganic Frameworks with Coordinatively Unsaturated Metal Sites in Storage and Separation of Methane and Carbon Dioxide, *J. Mater. Chem.*, 2009, **19**, 7362-7370.
- (15) T. Remy, S. A. Peter, S. V. Perre, P. Valvekens, D. E. D. Vos, G. V. Baron, F. Joeri and M. Denayer, Selective Dynamic CO₂ Separations on Mg-MOF-74 at Low Pressures: A Detailed Comparison with 13X, *J. Phys. Chem. C*, 2013, **117**, 9301-9310.
- (16) T. D. Kühne, M. Iannuzzi, M. D. Ben, V. V. Rybkin, P. Seewald, F. Stein, T. Laino, R. Z. Khaliullin, O. Schütt, F. Schiffmann, D. Golze, J. Wilhelm, S. Chulkov, M. H. BaniHashemian, V. Weber, U. Borstnik, M. Taillefumier, A. S. Jakobovits, A. Lazzaro, H. Pabst, T. Müller, R. Schade, M. Guidon, S. Andermatt, N. Holmberg, G. K. Schenter, A. Hehn, A. Bussy, F. Belleflamme, G. Tabacchi, A. Glöß, M. Lass, I. Bethune, C. J. Mundy, C. Plessl, M. Watkins, J. VandeVondele, M. Krack and J. Hutter, CP₂K: An electronic structure and molecular dynamics software package - Quickstep: Efficient and accurate electronic structure calculations, *J. Chem. Phys.*, 2020, **152**, 194103-194150.
- (17) J. P. Perdew, Density-functional approximation for the correlation energy of the inhomogeneous electron gas, *Phy. Rev. B*, 1986, **33**, 8822-8824.
- (18) J. P. Perdew, K. Burke, and M. Ernzerhof, Generalized Gradient Approximation Made Simple, *Phys. Rev. Lett.*, 1996, **77**, 3865–3868.

-
- (19) J. VandeVondele, J. Hutter, Gaussian basis sets for accurate calculations on molecular systems in gas and condensed phases, *J. Chem. Phys.*, 2007, **127**, 114105.
- (20) S. Goedecker, M. Teter and J. Hutter, Separable dual-space Gaussian pseudopotentials, *Phys. Rev. B*, 1996, **54**, 1703.
- (21) S. Grimme, J. Antony, S. Ehrlich and H. Krieg, A consistent and accurate *ab initio* parametrization of density functional dispersion correction (DFT-D) for the 94 elements H-Pu, *J. Chem. Phys.*, 2010, **132**, 154104.
- (22) C. Campana, B. Mussard and T. K. J. Woo, Electrostatic Potential Derived Atomic Charges for Periodic Systems Using a Modified Error Functional, *Chem. Theory Comput.*, 2009, **5**, 2866–2878.
- (23) D. Golze, J. Hutter and M. Iannuzzi, Wetting of water on hexagonal boron nitride@Rh(111): a QM/MM model based on atomic charges derived for nano-structured substrates, *Phys. Chem. Chem. Phys.*, 2015, **17**, 14307–14316.
- (24) S. L. Mayo, B. D. Olafson and W. A. Goddard, DREIDING: A Generic Force Field for Molecular Simulations, *J. Phys. Chem.*, 1990, **94**, 8897-8909.
- (25) J. G. Harris and K. H. Yung, Carbon Dioxide's Liquid-Vapor Coexistence Curve and Critical Properties As Predicted by a Simple Molecular Model, *J. Phys. Chem.*, 1995, **99**, 12021.
- (26) M. G. Martin and J. I. Siepmann, Transferable Potentials for Phase Equilibria. 1. United-Atom Description of *n*-Alkanes, *J. Phys. Chem. B*, 1998, **102**, 2569-2577.
- (27) D. Dubbeldam, S. Calero, D. E. Ellis and R. Q. Snurr, RASPA: molecular simulation software for adsorption and diffusion in flexible nanoporous materials, *Mol Simulat.*, 2016, **42**, 81-101.
- (28) D.-Y. Peng and D. B. Robinson, A New Two-Constant Equation of State, *Ind. Eng. Chem. Fundam.*, 1976, **15**, 59.

-
- (29) T. J. H. Vlugt, E. García-Pérez, D. Dubbeldam, S. Ban and S. Calero, Computing the Heat of Adsorption Using Molecular Simulations: The Effect of Strong Coulombic Interactions, *J. Chem. Theory Comput.*, 2008, **4**, 1107-1118.
- (30) T. D. Kühne, M. Iannuzzi, M. D. Ben, V. V. Rybkin, P. Seewald, F. Stein, T. Laino, R. Z. Khaliullin, O. Schütt, F. Schiffmann, D. Golze, J. Wilhelm, S. Chulkov, M. H. B. Hashemian, V. Weber, U. Borstnik, M. Taillefumier, A. S. Jakobovits, A. Lazzaro, H. Pabst, T. Müller, R. Schade, M. Guidon, S. Andermatt, N. Holmberg, G. K. Schenter, A. Hehn, A. Bussy, F. Belleflamme, G. Tabacchi, A. Glöß, M. Lass, I. Bethune, C. J. Mundy, C. Plessl, M. Watkins, J. VandeVondele, M. Krack and J. Hutter, CP2K: An electronic structure and molecular dynamics software package - Quickstep: Efficient and accurate electronic structure calculations, *J. Chem. Phys.*, 2020, **152**, 194103-194150.
- (31) S. Grimme, J. Antony, S. Ehrlich and H. J. Krieg, A consistent and accurate *ab initio* parametrization of density functional dispersion correction (DFT-D) for the 94 elements H-Pu, *Chem. Phys.*, 2010, **132**, 154104.
- (32) J. P. Perdew, Density-functional approximation for the correlation energy of the in homogeneous electron gas, *Phys. Rev. B*, 1986, **33**, 8822.
- (33) J. VandeVondele and J. Hutter, Gaussian basis sets for accurate calculations on molecular systems in gas and condensed phases *J. Chem. Phys.*, 2007, **127**, 114105.
- (34) S. Goedecker, M. Teter and J. Hutter, Separable dual-space Gaussian pseudopotentials. *Phys. Rev. B.*, 1996, **54**, 1703.
- (35) J. Ye and J. K. Johnson, Design of Lewis Pair-Functionalized Metal Organic Frameworks for CO₂ Hydrogenation, *ACS Catal.*, 2015, **5**, 2921-2928.
- (36) M. J. Frisch, G. W. Trucks, H. B. Schlegel, G. E. Scuseria, M. A. Robb, J. R. Cheeseman, G. Scalmani, V. Barone, B. Mennucci and G. A. Petersson, *Gaussian 09, Revision D.01,;Revision B.01,; Gaussian, Inc.:* Wallingford CT, **2010**.